

## Chapter 5

# Particle Deposition

As underlined in the introductory chapter of this thesis, the transport and eventual deposition of colloidal particles flowing through porous media is a phenomenon of great importance in both natural systems and for many industrial applications. In all these cases, the possibility of employing reliable mathematical models for the simulation of colloidal particle transport and deposition in porous media is particularly interesting, and often needed. In order to describe large spatial domains the models have to ignore the micro-porous structure of the medium and must be derived from an averaging procedure. The final macro-scale models result in different submodels for the each phenomenon involved and this work focuses on one of them: the rate of particle deposition on the surface of the grains constituting the porous medium. The commonly used theoretical framework for treating deposition of colloidal particles onto stationary collectors is the classic colloid filtration theory (CFT) (Nelson and Ginn, 2005). CFT describes fluid flow and particle deposition in porous media and is based on seminal work by Happel (1958), Levich (1962) and Kuwabara (1959), as described in more detail in Chapter 2. Some of these models have become very popular, as for example the Happel model, that has been used in many works (Tufenkji and Elimelech, 2004; Elimelech, 1991; Rajagopalan and Tien, 1976) even in derivative forms, some of which developed upon the sphere-in-cell model while retaining many of its features (Ma et al., 2010; Ma and Johnson, 2010), while others only use the simplicity of the spherical model as a starting point to develop more physical investigations (Cushing and Lawler, 1998; Johnson et al., 2007). Hydrodynamics and particle deposition for a number of different systems, namely the rotating disk, parallel-plate channel and for

---

The content of this chapter, in a modified form, has been published in Boccardo et al. (2014b)

stagnation point flow have also been studied (Elimelech, 1994). The difficulties in investigating these issues from the experimental point of view have prevented the development of accurate corrections to account for the presence of many grains (collectors) of irregular (i.e.: highly non-spherical) shapes and characterized by wide grain size distributions. Nowadays, the advancement of detailed mathematical models based on computational fluid dynamics (CFD) offers an interesting alternative to experimental investigation: some pore-scale simulations of physical packing of spheres (Long and Hilpert, 2009) and uniformly-sized flattened half-spheres have recently been performed (Long et al., 2010).

The objective of the work of this chapter is therefore to improve the current understanding of particle transport and deposition in porous media, by means of more detailed CFD simulations. In the micro-scale simulations small but representative portions of several porous media are considered and the details of the porous structure included. Many different representations of grain packings are investigated, in order to explore the influence of porosity, grain size and shape values. Some of the geometries used in this work were also successfully used in a recent study of pore-scale flow of non-Newtonian fluids in porous media (Tosco et al., 2013), and are similar to those employed by other authors in similar studies (Keller and Auset, 2007). First fluid flow is described by solving the continuity and Navier-Stokes equations, since particles are assumed to follow the flow, and results are compared with theoretical predictions of flow in porous media. Then, under the hypothesis of clean-bed filtration, particle deposition is investigated with focus on Brownian and steric interception mechanisms. Particular attention is devoted to the quantification of the effect of the irregularity of the grains and of the presence of multiple grains (or collectors) in the packing.

## 5.1 Test cases and operating conditions

In this work, Eqs. (2.1 - 2.14) are solved, in steady state conditions, on two sets of two-dimensional geometric porous medium models and results are then interpreted by using the theoretical models reported in Eqs. (2.5 - 2.36). The first set is composed of four randomly arranged distributions of non-overlapping identical circular elements, with their placement calculated via an appropriate algorithm (see Fig. 5.1a). The second set is constituted of eight realistic geometries with irregularly shaped and polydispersed grains (see Fig. 5.1b). The various cases for each of these sets represent porous media characterized by different values of mean grain diameter,  $d_g$ , and porosity,  $\varepsilon$ . A total of 12 geometries were necessary in order to provide for

a large enough field of investigation.

The first four synthetic cases were made via a simple brute-force algorithm that sequentially placed the items in random locations, each time checking for possible contacts with the other items already in place, repeating the step if necessary: thus preventing any overlap between them. The source for the eight realistic geometries were instead as many SEM (Scanning Electron Microscopy) images of real sand samples, which were treated in order to be transformed in geometric structures compatible for the use in a CFD code. The rationale behind the choice of these two different types of models (i.e., irregular versus circular grains) is to investigate two different situations: one that more closely resembles reality, and a more simplified one in which there is no effect of grain polydispersity and irregularities. In this way, it will be possible to study the influence of grain size distribution and shape on particle transport and deposition.

Since porosity ( $\varepsilon$ ) is an important parameter with respect to packed bed collector efficiency, we considered a wide range for this variable (0.3-0.5) in order to gain better insight with respect to its influence on particle removal efficiency. A similar choice (although in a complementary range 0.28-0.38) was made in recent works (Pazmino et al., 2011) which also highlighted the strong influence of porosity and grain size distribution on particle deposition. The final 12 geometries resulted also in nominal grain size  $d_g$  from 200  $\mu\text{m}$  up to 650  $\mu\text{m}$ , as detailed in Tab. 1. Figure 5.2 reports instead the nominal grain size distribution for some selected cases. The nominal grain size was estimated for those two-dimensional models from the specific surface area,  $s$ , of the porous medium:  $D_g = 4/s$ .

Table 1 also reports the spatial extent in the flow direction ( $L_x$ ) of the 12 geometries, excluding the premixing and postmixing zones added to improve the accuracy of the solution of the flow field and to reduce the impact of the backflow. In fact in order to minimize anomalous flow recirculations caused by the irregular nature of the packings, and to get a more accurate solution for the flow field (i.e.: less influenced by boundary effects), the length of these geometries was extended by adding two new “buffer” zones, before the inlet and after the outlet, as shown in Fig. 5.1.

After having built the 12 geometries, GAMBIT 2.4.6 was used to generate suitable meshes for the CFD code. Two-dimensional, quadrilateral, unstructured meshes were generated, minimizing cell skewness and aspect ratio. Then the meshes were refined uniformly and on the grain borders to fully resolve the momentum and particle concentration boundary layers. In Fig. 5.3 an example of a typical mesh near the border of a grain, as it undergoes the refining process, is reported.

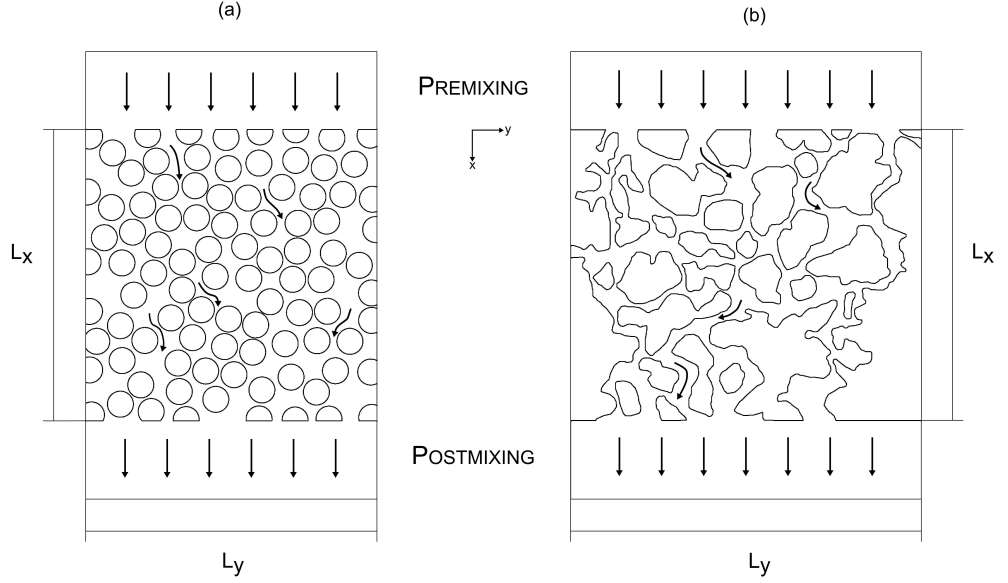


**Figure 5.1:** Sketch of the synthetic (left) and realistic (right) porous medium models investigated in this work.

Case	Geometry Type	$\varepsilon$ , -	$d_g$ , $\mu\text{m}$	$L_x \times L_y$ , mm
S1	Synthetic	0.418	205	$2.05 \times 2.05$
S2		0.464	206	$2.24 \times 2.24$
S3		0.404	309	$3.07 \times 3.07$
S4		0.458	308	$3.36 \times 3.36$
R1	Realistic	0.339	328	$2.69 \times 2.32$
R2		0.352	358	$2.69 \times 2.23$
R3		0.433	413	$2.69 \times 2.32$
R4		0.489	381	$2.69 \times 2.32$
R5		0.326	644	$6.65 \times 5.75$
R6		0.405	514	$6.65 \times 5.74$
R7		0.469	471	$5.56 \times 5.75$
R8		0.488	367	$4.75 \times 5.74$

**Table 5.1:** Porosity, nominal grain size ( $\mu\text{m}$ ) and domain extension (mm) for the synthetic geometries (first four rows) and the realistic geometries (subsequent eight rows).

One parameter was used to assess the grid independence of the results for the flow field. In order to obtain this single parameter for each geometrical model and for all the flow rates investigated (with particular attention to the momentum boundary layer near the grain border), pressure drop data from

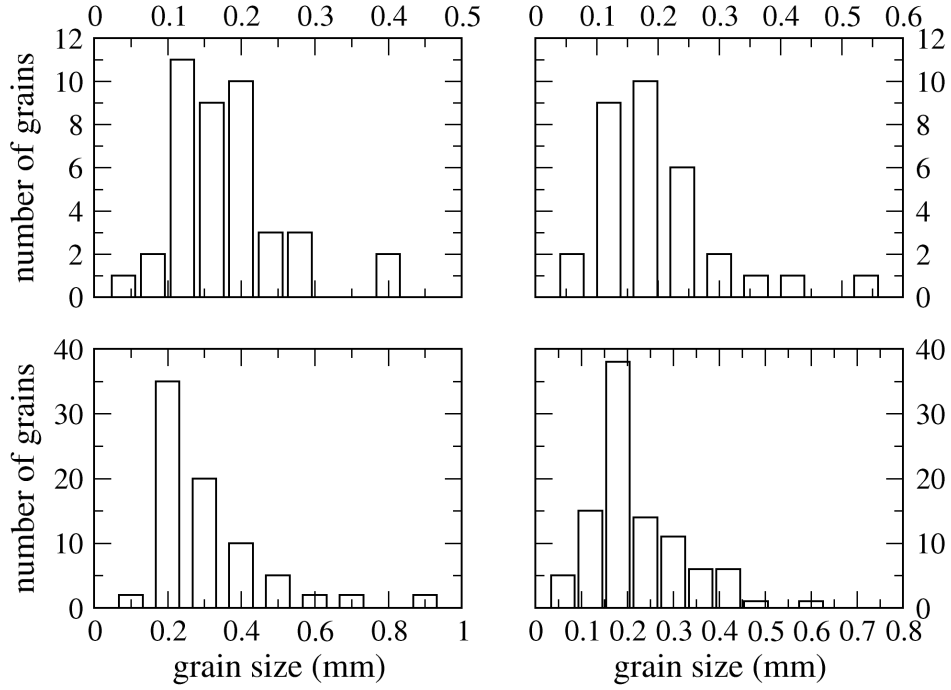


**Figure 5.2:** Grain size distribution for geometries (left to right and top to bottom): R1, R2, R6, R8.

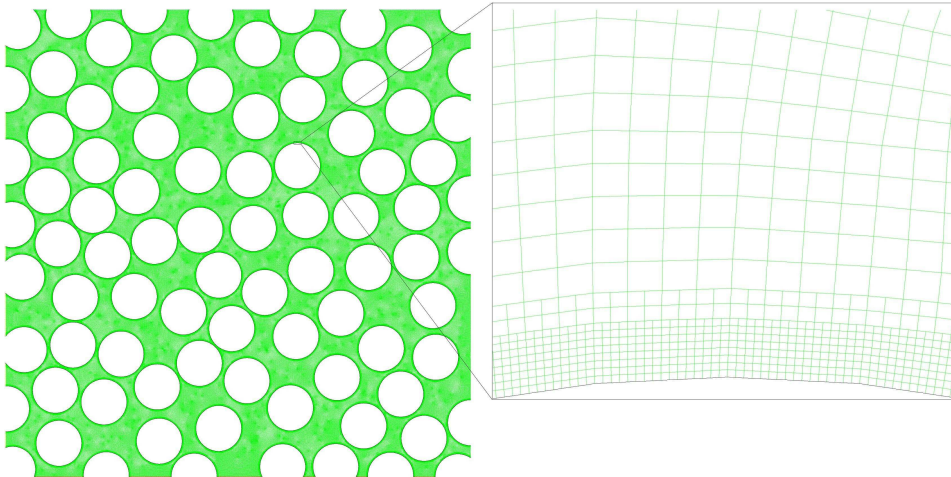


**Figure 5.3:** Particular of a mesh, showing the series of grid refinements.

the simulations were analyzed using the Ergun law, reported in Eq.(2.13).

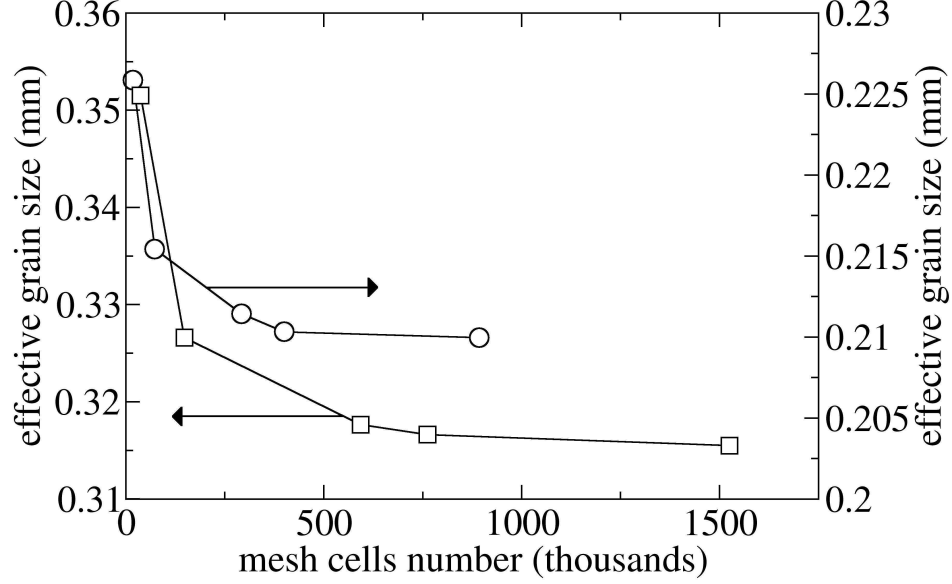


**Figure 5.4:** Effective grain size,  $d_g^*$ , with varying number of mesh cells, cases R1 (○) and S3 (□).

These results were then fitted to this law, in order to obtain a new equivalent or effective grain size,  $d_g^*$ . As it can be seen in Fig. 5.4, where the variation of  $d_g^*$  increasing the mesh cell number is reported (starting from the original cell number), grid independent flow field results are obtained for the second (uniform) refinement. It is therefore possible to conclude that the corresponding grid fully describes the momentum boundary layer.

The boundary layer of particle concentration required a finer mesh (near the grains) due to the resulting Schmidt number (Asano, 2006), especially for the larger particles. Grid-independence for particle transport and deposition will be, for clarity, discussed later on, and Tab. 2 reports the final number of mesh cells for the 12 investigated cases.

The system is considered isothermal at  $T = 293\text{ K}$ , and the fluid is Newtonian (density  $\rho = 998,2\text{ kg m}^{-3}$  and dynamic viscosity  $\mu = 0,001003\text{ kg m}^{-1}\text{ s}^{-1}$ ). The flow is considered laminar, and thus the CFD code did not solve additional turbulence models. This is justified given the range of velocities explored: in fact, the superficial velocities,  $U$ , ranged from  $10^{-6}$  to  $10^{-1}\text{ m s}^{-1}$  (roughly corresponding to  $\text{Re}^*$  ranging from  $10^{-4}$  to 10).

As for the boundary conditions for these cases, an inlet zone was set on one side of the geometry, where water flowed into the domain at a fixed velocity, and the outlet at the opposite side. This setup aims to represent a

Case	Mesh cells (thousands)
S1	894
S2	1 058
S3	1 525
S4	1 840
R1	893
R2	884
R3	816
R4	642
R5	1 950
R6	2 254
R7	1 828
R8	1 931

**Table 5.2:** Final number of mesh cells for the synthetic geometries (first four rows) and the realistic geometries (subsequent eight rows).

situation in which the fluid is moving predominantly in one direction, and as such the simplest and most appropriate way to reconstruct the large-scale system with a smaller, representative domain is to align the flow direction with one of the three main cartesian axis, resulting in the two sides orthogonal to that axis to be respectively the inlet and outlet boundaries of the domain. It has to be noted that gravity was not considered in our model and its effect was not accounted and solved for in the CFD calculations, thus ignoring the influence of sedimentation on particle deposition. This results implicitly in considering  $\eta_G = 0$ . On the two remaining sides a condition of symmetry was set. This condition ensures that all property fluxes are equal to zero along the specified border, resulting in no fluid flow across these boundaries. Regarding the interpretation of the results, those of most interest refer to the pressure drop, which was calculated as the difference between the inlet and outlet boundary values. After normalizing on the length of the domain ( $\Delta P/L_x$ ), the results for the cases at small superficial velocity was used to estimate the permeability of the porous media  $k = U \mu \Delta P/L_x$ . Pressure drop results were also compared with the predictions of the Ergun law, as explained earlier.

As for particle deposition, only Brownian motions and interception were considered, for different populations of monodispersed particles, with diameters,  $d_p$ , equal to 1, 10, 100, 200, 500, 625, 750, 875 nm and 1  $\mu\text{m}$ . The presence of the particles flowing into the domain with the fluid was simulated by representing them with a scalar, namely the normalized particle concentration,  $C$ . Initially the particle deposition velocity was calculated

with a two-fluid Eulerian multiphase model, however, in the range of operating conditions considered in this work particle velocity always relaxed to the fluid velocity. This result was to be expected since, as explained earlier, both Stokes numbers for all considered cases are very low, and viscous drag forces causing hydrodynamic retardation were not considered in our simulation framework, thus the assumption of one-way coupling between particle and fluid, with the velocity of the former always relaxing to that of the latter; moreover, the typical particle concentration is low enough not to have any two-way coupling. Brownian motions were accounted for by the diffusive term of Eq. (2.14), with the diffusivity coefficient calculated with the Einstein-Stokes relationship reported in Eq.(2.15). While diffusivity of particles could be anisotropic and in general will vary between the bulk of the fluid and near the borders of the solid grains, here it will be considered constant.

The boundary conditions for this normalized concentration scalar were set to one at the inlet, with diffusive flux at the outlet set to zero. Regarding the initial conditions, in all cases scalar concentration was set to zero in all the domain, as it provided for a smoother and faster convergence of the numerical solution with respect to other initialization values.

The last fundamental boundary condition is imposed at the grain borders. As described earlier, since in this work we are interested in evaluating the deposition efficiency,  $\eta_0$ , all the repulsive forces responsible for the reduction of the attachment efficiency,  $\alpha$ , were ignored (making  $\alpha = 1$ ), which translates into setting a particle concentration at the border of the grains equal to zero. To account for interception caused by steric effects due to the finite size of the particle, a user-defined function (UDF) was used to set to zero the particle concentration in all the mesh cells whose centroids' distance from the grain wall was less than the particle radius. In practice, the UDF shifts the grain boundary by a distance equal to the particle radius. It has to be noted that the lengths involved are very small, representing yet another reason for the need for a finer grid at the grain border. The final grid sizes, reported in Tab. 2, are however reasonable, since interception is only significant for large particles.

From these simulations the value of particle concentration in the microscale domain is obtained. Our objective is to extract from this information, i.e.  $C(x, y)$ , a macroscopic model with which to calculate the particle deposition rate without describing the details of the pores. As it has been said, the fluid moves mainly from the inlet to the outlet, and it is thus along this direction that a meaningful particle concentration gradient will be identifiable. More specifically, it is useful to express the results as the difference



in concentration between the porous inlet and outlet zones. First then, the concentration value at any point along the porous bed is averaged in the direction orthogonal to the flow ( $0 < y < L_y$ ):

$$\hat{C}(x) = \frac{1}{L_y} \int_0^{L_y} C(x, y) dy . \quad (5.1)$$

The concentration at the inlet and outlet boundaries, equal to  $\hat{C}(x = 0)$  and  $\hat{C}(x = L_x)$ , is readily available from our CFD simulations. From these, a simplified description which ignores pore details but results in the same overall deposition rate can be obtained simply by using the following deposition efficiency (in the case of  $\alpha = 1$ ):

$$\eta_0 = \frac{\ln\left(\frac{C_0}{C}\right)}{-\frac{3}{2}\left(\frac{1-\varepsilon}{\varepsilon}\right)\left(\frac{L_x}{d_g}\right)} , \quad (5.2)$$

where again  $C_0 = \hat{C}(x = 0)$  and  $C = \hat{C}(x = L_x)$  are obtained from CFD simulations. A preliminary test case was set up, in order to validate the methodology used both in the CFD simulations and in the analysis of the results. The system chosen as a benchmark was Levich case of diffusion on a free-falling solid sphere, for the simplicity of its geometrical model and for its solution resulting surely from an analytical derivation. Results from simulations replicating this model and ran in operating conditions inside the range of validity of the Levich model were then compared with the theoretical predictions of Eq. (2.27). The outcome was positive, as the coefficients of the power law describing the CFD results showed a remarkable accordance with Eq. (2.27), thus ensuring the appropriateness of the methodology used in this work for treating this kind of systems.

Summarizing, the following strategy was used. First, simulations with only the Brownian diffusion mechanism accounted for were run, resulting in the Brownian deposition efficiency  $\eta_B$ . Secondly, both Brownian motion and interception mechanisms were considered resulting in the overall deposition efficiency  $\eta_0$ . Subsequently  $\eta_I$  was calculated by inverting Eq. (2.36) (keeping in mind that in our case,  $\eta_G = 0$ ). Eventually the relationship between  $\eta_B$  (and  $\eta_I$ ) and  $U, \varepsilon, d_g^*$  and  $d_p$ , was assessed by running simulations at several superficial velocities,  $U$ , for the porous media (characterized by several porosity,  $\varepsilon$ , and effective grain size,  $d_g^*$ , values) previously described and with different particle sizes,  $d_p$ .

## 5.2 Results and discussion

In this section the results obtained from simulations run on the grids reported in Tab. 2 are discussed. First, values of pressure drops in the domain were calculated and used to estimate the permeability of the system. As well known, Darcy's law has an upper range of validity (in terms of Reynolds number) beyond which the relationship between pressure drop and fluid velocity is not linear anymore: typical values of  $Re^*$  for this transition are of the order of unity (Hassanizadeh and Gray, 1987). These considerations are confirmed in Fig. 5.5, where values of the group  $q\mu/(\Delta P/L_x)$  (equal to permeability for low  $Re$ ) are reported in a logarithmic scale against  $q$  and labeled with the corresponding  $Re$  values. As it can be clearly seen this group is characterized by a constant value up to  $Re \approx 1$  (corresponding to  $q$  of about  $10^{-2} \text{ m s}^{-1}$  for these two cases), after which it undergoes a sharp decrease, for both the realistic and the synthetic geometries.

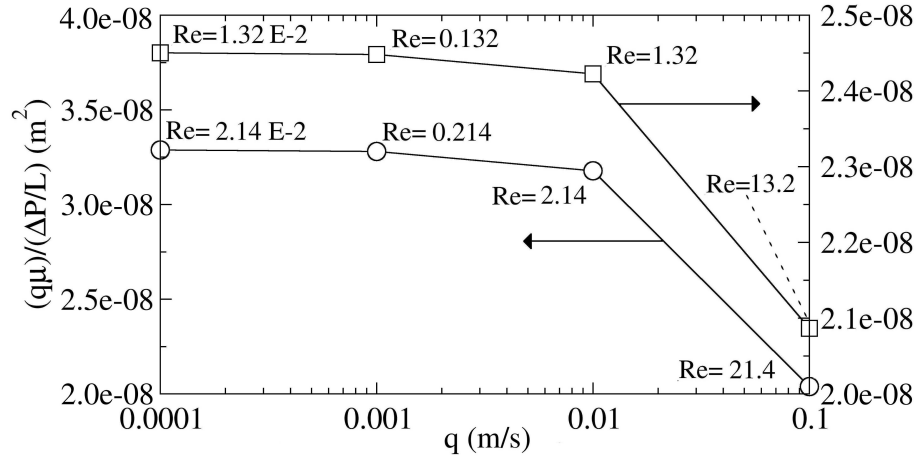


**Figure 5.5:** Values of the group  $q\mu/(\Delta P/L_x)$ , case R1 (○) and S1 (□).

The next step in analyzing fluid flow results is to compare pressure drop values obtained from simulations with Ergun's law predictions calculated with the nominal grain size,  $d_g$ . As it can be seen in Fig. 5.6 (left), the qualitative behaviour of  $\Delta P^*$  versus  $Re^*$  follows the theoretical predictions, with a large displacement with respect to the theoretical law. By fitting the Ergun law (see Fig. 5.6, right), the modified or effective grain diameter,  $d_g^*$ , is calculated. As already explained this is done by fitting the value of  $d_g$ , appearing in Eq. (2.12) in order to reduce the distance between the CFD

simulation data and the Ergun's law predictions to less than 10% in value, moving from Fig. 5.6 (left) to Fig. 5.6 (right). In Table 3 the values of the original grain diameter  $d_g$  and the equivalent diameter resulting from fitting the Ergun law are compared. While there is a difference between  $d_g$  and  $d_g^*$  in the case of the eight realistic geometries, values are much closer for the four synthetic geometries. Finally, qualitative description of the flow field can be found in Fig. 5.7.

Label	$d_g$	$d_g^*$
S1	205	133
S2	206	143
S3	309	315
S4	308	291
R1	328	215
R2	358	210
R3	381	179
R4	413	178
R5	644	224
R6	514	198
R7	471	215
R8	367	123

**Table 5.3:** Original and fitted equivalent grain size, for synthetic geometries (first four rows) and realistic geometries (subsequent eight rows)

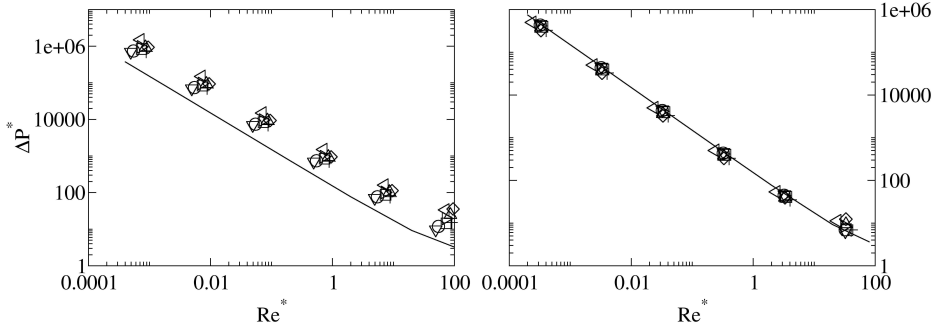


**Figure 5.6:** Comparison of CFD results (symbols) with Ergun's law (continuous line).

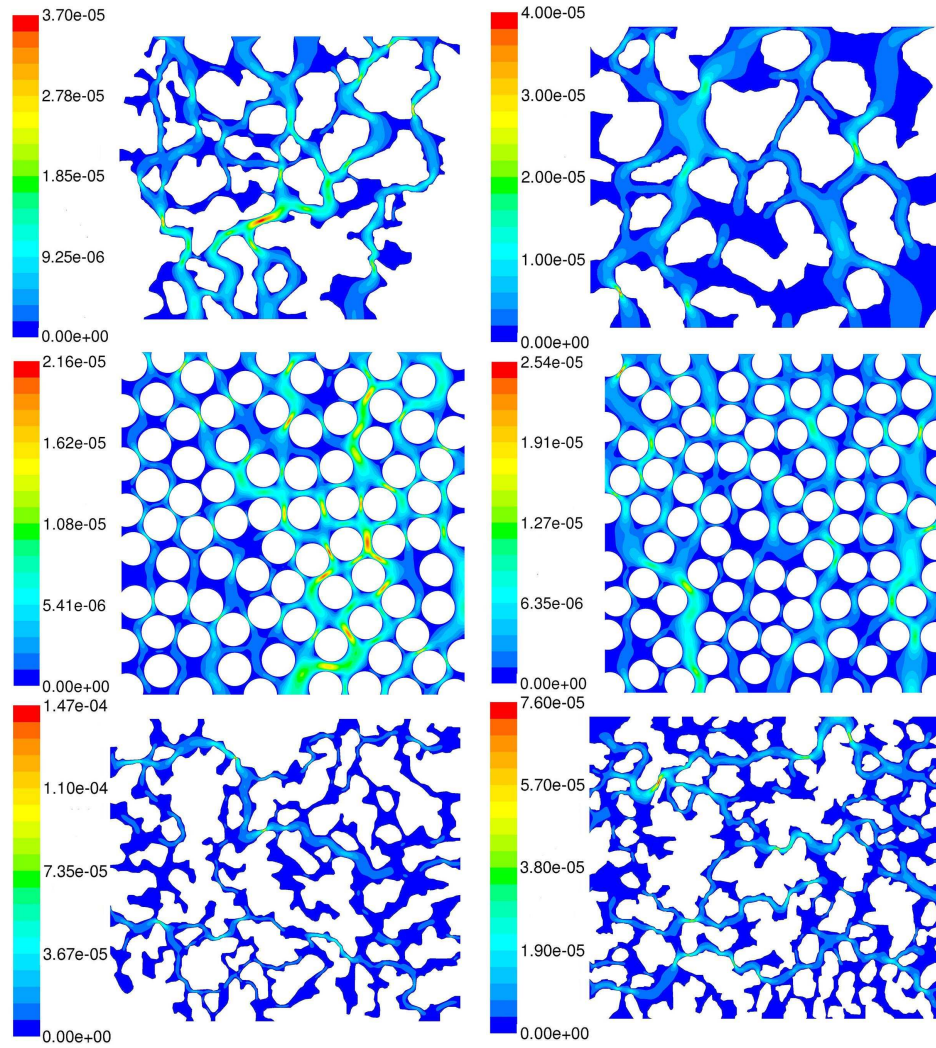


**Figure 5.7:** Contour plots of fluid velocity ( $ms^{-1}$ ) for cases (left to right and top to bottom): R2, R4, S1, S2, R5, R6, for superficial velocity  $q = 10^{-6} ms^{-1}$ .

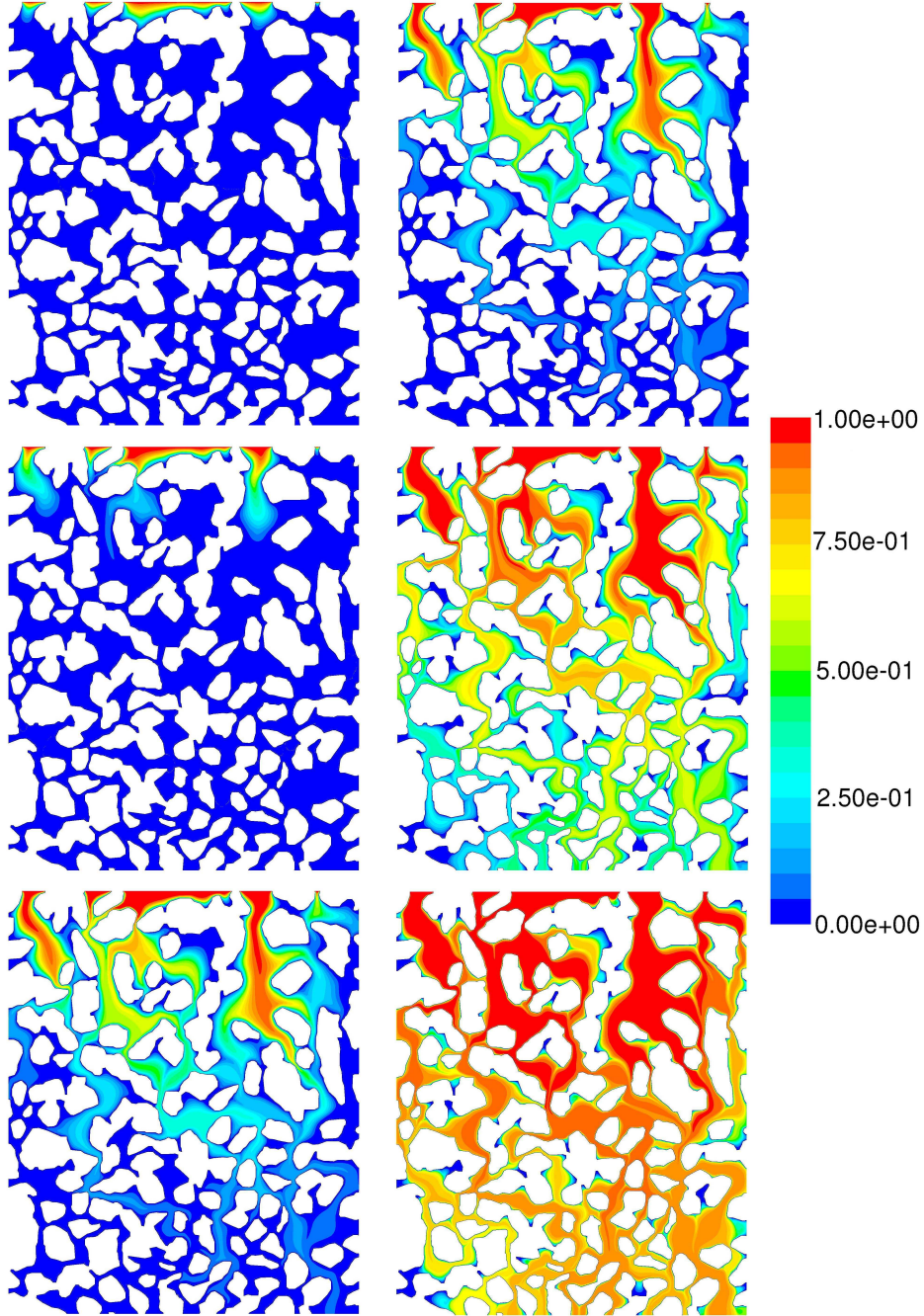


**Figure 5.8:** Contour plots of normalized particle concentration for case R8, for  $q = 10^{-6} \text{ ms}^{-1}$  (first row),  $q = 10^{-5} \text{ ms}^{-1}$  (second row),  $q = 10^{-4} \text{ ms}^{-1}$  (third row), for  $d_p = 1 \text{ nm}$  (first column) and  $d_p = 100 \text{ nm}$  (second column).



After having investigated the flow in the system, particle deposition was simulated as previously explained. Contour plots of particle concentration for one case are reported in Fig. 5.8. As explained, from these results the overall deposition efficiency,  $\eta_0$ , is calculated with Eq. (5.2), and plotted versus fluid velocity ( $10^{-6} < q < 10^{-2} \text{ m s}^{-1}$  corresponding to  $10^{-4} < \text{Re}^* < 1$ ) and particle size in Fig. 5.9.

Figure 5.9 clearly shows how the deposition rate (and consequently,  $\eta_0$ ) progressively decreases as the superficial velocity is increased (for small particles). This is due to the time scale of convective transport becoming smaller with respect to diffusive transport; in fact, particles at higher velocities have less time to reach the grain borders (and thus to be removed) from the bulk of the fluid. The behaviour changes for particles of about 500 nm and larger, as  $\eta_0$  initially decreases but then stays approximately constant. This is due to the effect of steric interception, which has a higher impact on deposition velocity only for larger particles (on the contrary of Brownian diffusion which acts predominantly at smaller particle sizes) and for higher fluid velocities, when the effect of Brownian deposition becomes negligible. The same data (for the same parameters) is represented in Fig. 5.10, where the deposition efficiency,  $\eta_0$ , is now plotted versus particle size,  $d_p$ , at different superficial velocities  $q$ . As already discussed, for the lower superficial velocities the particle deposition efficiency always decreases as the particle size is increased, while for higher velocities the particle deposition initially decreases for small particle sizes and instead sees a positive slope for larger particles. In fact, for  $q$  larger than  $10^{-3} \text{ m s}^{-1}$  a minimum for  $\eta_0$  is detected at about 300 - 500 nm. Similar trends were experimentally observed (although in a slightly different porosity range) by other authors (Pazmino et al., 2011).

These results and the general considerations just made are consistent with the underlying theory and are valid both for the realistic and the synthetic geometries. There are, however, some differences between these two cases. In order to better highlight these differences, let us consider results for Brownian deposition efficiency only,  $\eta_B$ . In Fig. 5.11 the aggregate results of the overall deposition efficiency,  $\eta_0$ , normalized by the porosity-dependent function,  $As$ , of (2.34) are reported versus  $\text{Pe} = qd_g/\mathcal{D}$  for all the synthetic geometries. This normalization is done to compare data from different geometries.

First of all, it is interesting to highlight that when data corresponding to different synthetic geometries obtained under different superficial velocities and particle sizes are plotted versus the Péclet number, a single master curve is obtained, which is consistent with the theoretical predictions of Eq. (2.33). By fitting the results of our CFD simulations with an equation of

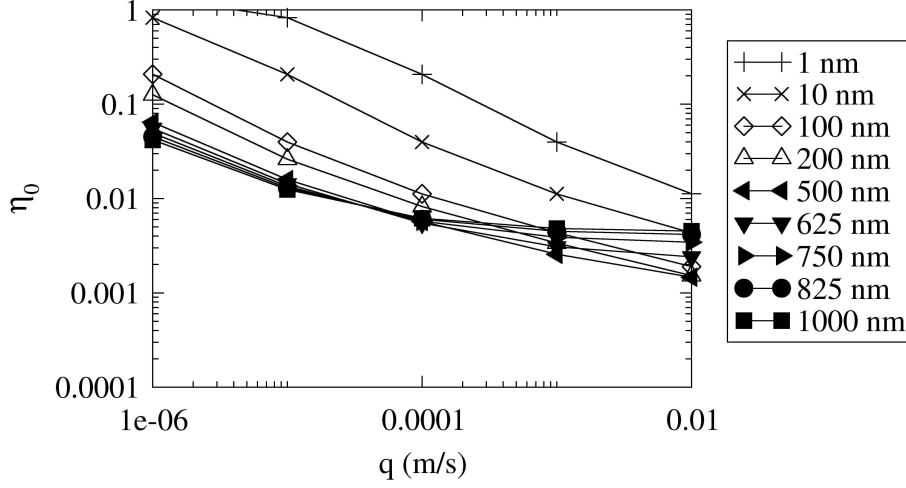


**Figure 5.9:** Particle deposition efficiency for case R1, at different fluid velocities and particle sizes.

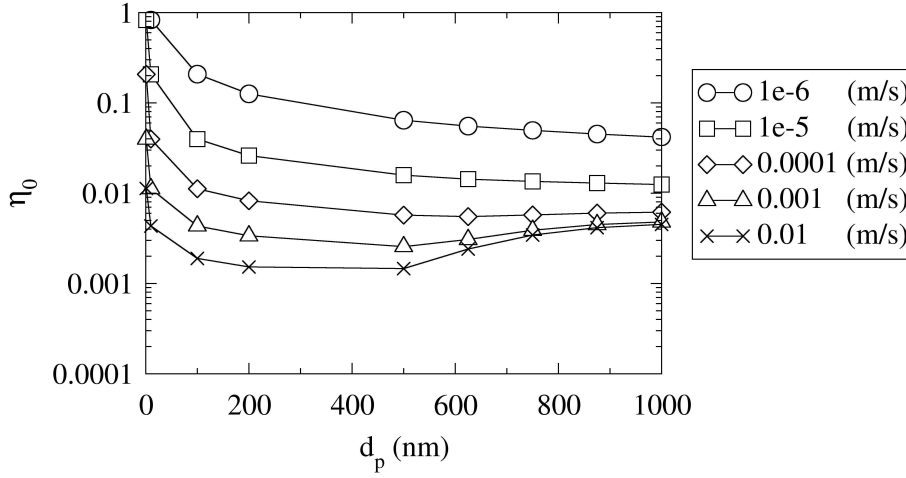


**Figure 5.10:** Particle deposition efficiency for case R1, at different fluid velocities and particle sizes.

the form:

$$\eta_B = C_1 A s^{\frac{1}{3}} \text{Pe}^{\beta}, \quad (5.3)$$

the following values  $C_1=0.487$  and  $\beta = -0.552$  are obtained. While the value of  $C_1$  is quite different from the theoretical (Pfeffer, 1964) value, a

small difference between  $\beta = -0.552$  and the  $-2/3$  exponent of the theoretical law, reported in Eq. (2.33), is detected. Regarding these deviations, it is interesting to note a recent work (Ma et al., 2013) which has shown in detail some of the shortcomings of correlation equations with a power-law dependence on Peclet number and of employing Eulerian models with Dirichlet boundary conditions for concentration (as is the case in this work), arising predominantly at very low fluid velocities. These findings can help to explain the presence, in Figs. 5.11 and 5.12 of values of  $\eta$  over unity. Moreover, since when one single circular collector is considered, as in the benchmark case of Levich, the original exponent is obtained ( $\beta = -2/3$ ) from our simulations, the difference can be attributed to the presence of many collectors in the porous medium, due to the interactions of the particle concentration boundary layers.

These two values of  $C_1$  and  $\beta$  are also used to assess grid independence of these results. As grid independence for flow field predictions was evaluated with the effective grain size,  $d_g^*$ , the grid independence of particle deposition predictions was assessed with the invariance of the fitted  $C_1$  and  $\beta$  values to further grid refinements. Results showed that using the meshes of Tab. 2 grid independence was achieved.

A different scenario emerges when looking at results of  $\eta_B$  versus  $Pe$  for the eight realistic geometries, shown in Fig. 5.12.

Comparison of Figs. 5.11 and 5.12 reveals two main differences: the first lies in the different coefficients for the power law  $\eta_B$  versus  $Pe$ , whereas the second one is the separation between the curves corresponding to different geometries, highlighting the imperfect collapse of the data into one single master curve for realistic grains. In fact, the fitted master curve for the synthetic grains (see Fig. 5.11) corresponds to a coefficient of determination ( $R^2$ ) of 0.9789, whereas that of the realistic grains (see Fig. 5.12) shows a much lower coefficient of determination, equal to 0.9141.

These deviations call for the search for another parameter (besides porosity and grain size) to be included in the predictive laws for Brownian particle deposition. In this work, possible influences of the tortuosity of the porous media and of other forms of the porosity-dependent term  $As$  were analyzed. In the first case, tortuosity of each system was estimated, via CFD simulations, by means of analyzing the residence time distribution function of an inert tracer flowing through the medium. In the second case, a search for a new porosity-dependent function was performed, with the aim of eliminating the offset seen in Fig. 5.12. This was done in practice by trying to find a constitutive equation that can correctly predict the value of  $\eta_B$  for different systems, at different values of  $Pe$ . Unfortunately, for both cases, no clear



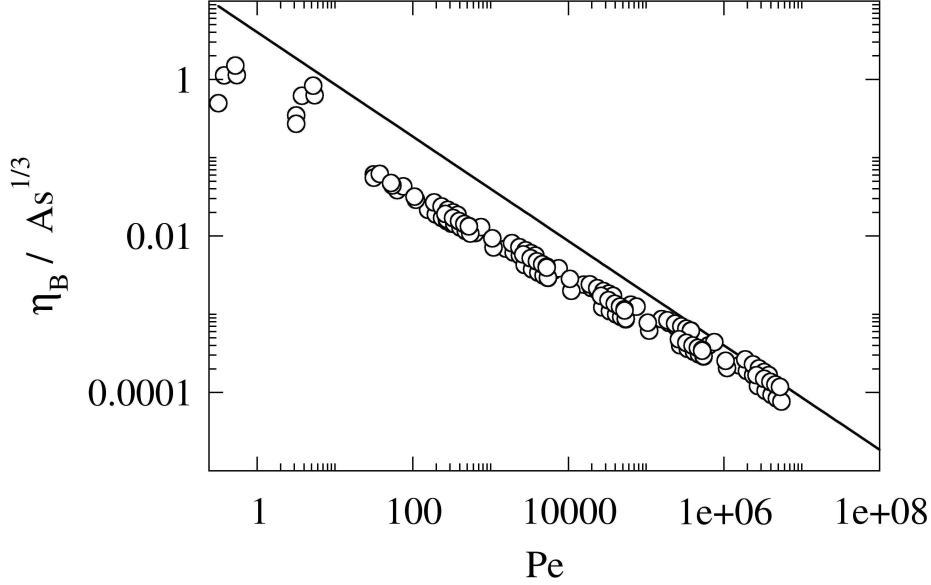


**Figure 5.11:** Brownian deposition efficiency  $\eta_B$  versus  $Pe$  for synthetic geometries, compared with the theoretical law (Eq. (17), continuous line).

relationship linking tortuosity to deposition efficiency, nor a new and more adequate form of  $As$ , could be found. It is also interesting to highlight here that the use of the Kuwabara function,  $g(\varepsilon)$ , of Eq. (2.32) instead of the porosity dependent function,  $As$ , of (2.34) led to very similar results.

Regarding the coefficients of the power law, and again referring to an equation of the form of Eq. (5.3), the values of  $C_1 = 0.1926$  and  $\beta = -0.52$  were found. As it can be seen, the coefficient  $\beta$  has a similar value with respect to results for the synthetic grids, while the value of  $C_1$  lies even further from the theoretical one. Even in this case the discrepancies can be attributed to the complex interactions between collectors that result in a very different overall behaviour.

Moreover, it has to be taken into account that our simulations were conducted with the same assumptions of the Smoluchowski-Levich approximations, valid only for particles smaller than a few hundred nanometers. Including the drag correction in the calculations would decrease the rate of collection with effects of increasing magnitude with increasing particle size (Rajagopalan and Tien, 1976; Spielman and Fitzpatrick, 1973). Quantitative comparisons between the inclusion of the drag corrections, or lack thereof, can be found in Rajagopalan and Tien (1976) and Prieve and Ruck-

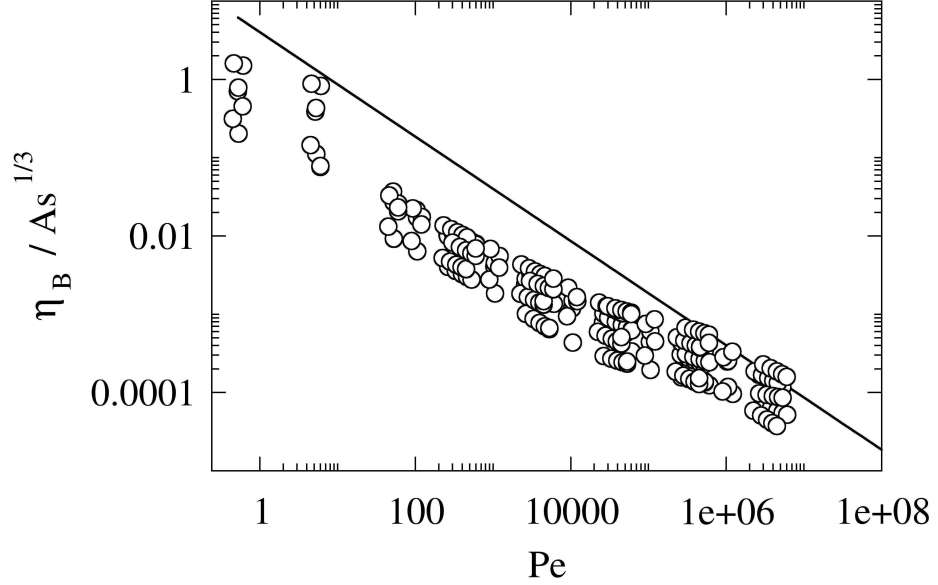


**Figure 5.12:** Brownian deposition efficiency  $\eta_B$  versus  $Pe$  for realistic geometries, compared with the theoretical law (Eq. (17), continuous line).

enstein (1974). The use of the Smoluchowski-Levich approximation in the case of large particles would lead to an overestimation of the collector efficiency. This is clearly shown in the work of Tufenkji and Elimelech (2004) which included the contribution of hydrodynamic retardation, obtaining a different exponent of the Péclet number in the equation for the Brownian deposition efficiency and also added a dependency on  $N_R$ , absent in the original Levich-Yao formulation. These findings are related to the influence of hydrodynamic interactions. Nonetheless, it has to be noted that the range of particle sizes explored in that work was considerably wider (up to  $10\ \mu\text{m}$ ), with hydrodynamic interactions influencing more the deposition efficiency for larger particles. In fact, when comparing their results with works not fully including hydrodynamic effects (Rajagopalan and Tien, 1976), the maximum of the difference (about 50%) was found at  $d_p = 2\ \mu\text{m}$ , with much lower discrepancies at smaller particle sizes. While it wouldn't be possible to provide an accurate estimate for the deviation between our results (based on the Smoluchowski-Levich approximation) and a more complete model, due to the presence of attractive forces which were also not explicitly included in our simulations and that would balance out, in a measure, the hydrodynamic retardation effect (Tufenkji and Elimelech, 2004; Adamczyk

et al., 1983), the indications found in these references call for greater care when interpreting results for particles in the 1- $\mu\text{m}$  range, and the possible dependence on a new term in the brownian deposition efficiency equation ( $N_R$ ) warrants for a deeper investigation of these phenomena.

Finally, interception results are also presented. In this case there are no clear differences between results of synthetic and realistic geometries. Figure 5.13 shows the results of  $\eta_I$  at different values of  $N_R$ , compared with the theoretical predictions of Eq. (2.35). For clarity of exposition, only results pertaining to case R3 are reported in Fig. 5.13, but very similar results were obtained for the other 11 cases. In this case it is clear that while the theoretical law restrains the interception effect as being dependent on the parameter  $N_R$ , defined as the ratio between grain diameter and particle size, our results show large deviations between cases corresponding to different fluid velocities. In this case, searching for a new and corrected predictive equation clearly points towards adding a dependence of  $\eta_I$  on the fluid velocity (or more properly, in order to retain a law dependant on dimensionless parameters, the Reynolds number), which would result in a form similar to the original law:

$$\eta_I = C_2 As N_R^2 \text{Re}^\gamma . \quad (5.4)$$

A least-squares fitting of these results returns a best value for  $C_2$  and  $\gamma$  respectively equal to 1.116 and 0.145. Even if the value for  $\gamma$  does not show a strong correlation between  $\text{Re}$  and  $\eta_I$ , it is nevertheless possible to obtain more accurate predictions of the interception effect on deposition with the new law, as shown in Fig. 5.14. Again, only results pertaining to case R3 are reported, for a clear comparison with Fig. 5.13, but it has to be noted that this least-squares fitting process, resulting in the  $C_2$  and  $\gamma$  reported above, has been performed not on this single geometry but on the aggregate of all the particle deposition efficiency results for all the geometries considered in this work. At last we highlight that interpreting the data with the other laws available in the literature reported in Eqs. (2.28) and (2.31), resulted in similar conclusions.

### 5.3 Conclusions

Particle transport and deposition in porous media was investigated in this work by means of detailed microscale CFD simulations. Firstly results were carefully analysed to assess grid independence. When considering one single

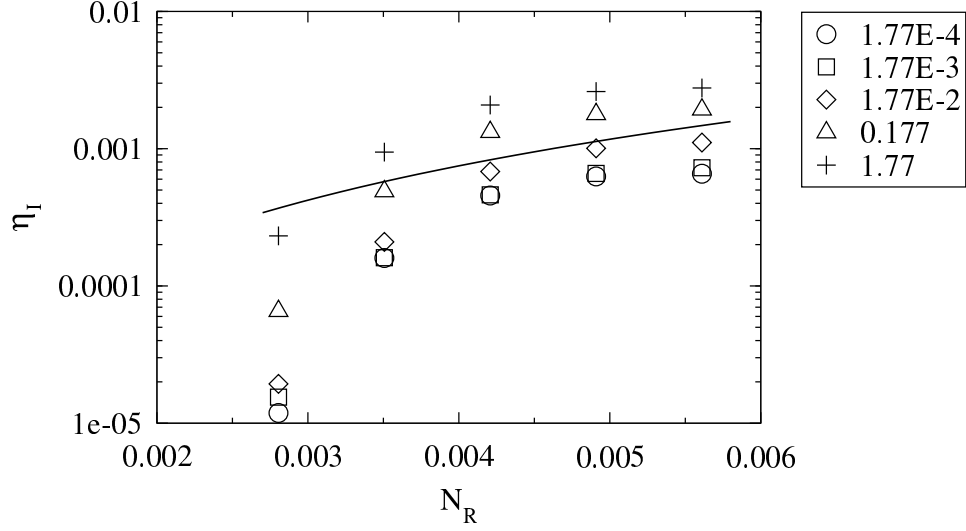


**Figure 5.13:** Interception deposition efficiency  $\eta_I$  results for case R3 varying the parameter  $N_R$  and for a range of Reynolds numbers (specified on the key) compared with the theoretical relationship Eq. (2.35) (continuous line).

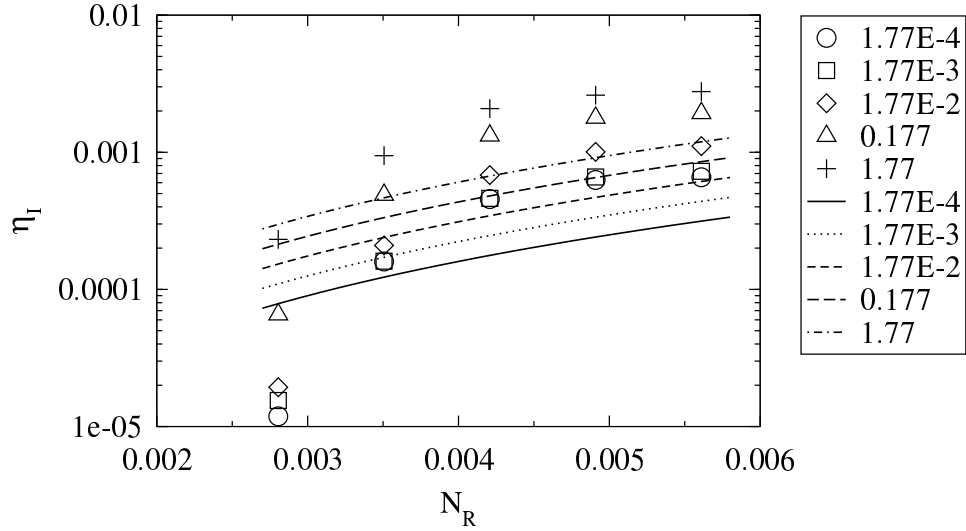


**Figure 5.14:** Interception deposition efficiency  $\eta_I$  results for case R3 varying the parameter  $N_R$  and for a range of Reynolds numbers (specified on the key) compared with the new modified relationship, obtained from fitting the aggregate results of all the geometries (continuous and dashed lines).

collector with Brownian motion as the dominant mechanism for deposition, the original correlation proposed by Levich was obtained:  $\eta_B = 4.04\text{Pe}^{-2/3}$ , thus proving the consistency of the methodology adopted with the underlying theory. When considering complex porous media constituted by dif-

ferent circular collectors an analogous dependency, characterised by a different slope:  $\eta_B = 0.487 As^{1/3} Pe^{-0.552}$ , was found. In this case porosity,  $\varepsilon$ , and effective grain size,  $d_g^*$ , were capable of fully characterizing the observed behaviour. In the case of irregular collectors a similar dependency was again observed ( $\eta_B = 0.1926 As^{1/3} Pe^{-0.52}$ ) although porosity,  $\varepsilon$ , and effective grain size,  $d_g^*$ , seem not to be capable alone to fully characterize the porous medium. In fact, comparing Figs. 5.11 and 5.12, the former shows a collapse of the results on a single master curve dependent on these two parameters, while the latter shows a clear separation of the results pertaining to each geometry. This is further highlighted by the very different coefficients of determination showed by the two obtained master curves, respectively equal to  $R^2=0.9789$  and  $R^2=0.9141$ . This deviation arising in the case of realistic geometries would seem to indicate that another parameter should be included in the laws predicting Brownian particle deposition. We are confident that the effect of the neglected hydrodynamic retardation on our results is small for nanometric particles, but might be more important (up to 50%), for micrometric particles. Therefore results for the largest particles investigated in this work should be treated with great care. When interception is also considered, the interaction between the particle boundary layers of the different grains create a complex dependency resulting in the following relationship:  $\eta_I = 1.116 As N_R^2 Re^{0.145}$ , valid for both circular and irregularly shaped collectors.



## Chapter 6

# Homogenization by multiple-scale expansion

As stated and demonstrated in the second chapter of this thesis, homogenization is a powerful and versatile tool for the upscaling of transport and reaction equations in porous and heterogeneous media. For example, Taylor dispersion in porous media has been approached in this way ([Auriault and Adler, 1995](#)), and a recent example in the literature deals with the problem of heterogeneous (surface) reaction ([Battiato and Tartakovsky, 2011](#)). Moreover, it is especially suited to the combination with microscale methods (e.g.: computational fluid dynamics) due to the necessity of obtaining a solution of the cell problem. A number of constraints to the homogenization of the chosen problem also arise during the procedure, usually in terms of ranges of operating conditions where the final upscaled equation will be employable. Having identified these regions, within the same theoretical framework (as demonstrated by [Battiato et al. \(2009\)](#)), it is then possible to set up hybrid pore-scale/homogenized simulations for a complete and robust treatment of the problem under investigation, at the relevant spatial scale.

Our objective is then to start from the same equations solved in the CFD model and obtain an employable macroscale formulation of the advection-diffusion-deposition problem. As it will be shown, only one simplifying assumption will be used in this respect, and that is the choice to restrict the range of fluid velocities to the Stokes' regime, thus solving the Stokes' equation of motion instead of the full Navier-Stokes equation. Then, we will consider an advection-diffusion equation with no explicit source term, and the surface deposition phenomenon will be introduced by setting a boundary condition of particle concentration equal to zero, as it was done in Chapter 5 and also used in the CFD simulations. Again, the purpose is to obtain

a macroscale predictive model for the particle removal rate by deposition which does not need to take into account the details of the medium microstructure.

## 6.1 Problem Formulation

We will consider a porous medium having a structure identical to the one described as a “medium with obstacles” in the Section 2.3.2 earlier in this thesis. That is, a macroscale structure  $\hat{\Omega}$  with characteristic length  $L$ , composed of spatially repeating unit cells  $\hat{Y}$  with characteristic length:  $l = \xi L \ll 1$ . As mentioned, we consider an incompressible fluid flowing at very low velocities, which is thus described by the Stokes and continuity equation in the fluid domain  $\hat{\mathcal{B}}^\xi$ , coupled with a no-slip condition on the grains walls,  $\hat{\Gamma}^\xi$ , as following:

$$\begin{cases} \hat{\mu} \hat{\nabla}^2 \hat{\mathbf{v}}_\xi - \nabla \hat{p}_\xi = 0 & \hat{\mathbf{x}} \in \hat{\mathcal{B}}^\xi \\ \hat{\nabla} \cdot \hat{\mathbf{v}}_\xi = 0 & \hat{\mathbf{x}} \in \hat{\mathcal{B}}^\xi \\ \hat{\mathbf{v}}_\xi = 0 & \hat{\mathbf{x}} \in \hat{\Gamma}^\xi \end{cases} \quad (6.1)$$

where  $\hat{\mu}$  is the fluid dynamic viscosity,  $\hat{\mathbf{v}}_\xi(\mathbf{x})$  its velocity and  $\hat{p}$  its pressure. The superscript  $\hat{\phi}$  means that  $\phi$  is a dimensioned variable (or differential operator applied on dimensioned variables). Then, we consider particle transport, governed by an advection-diffusion equation as Eq. (2.14), which we rewrite in the following form:

$$\begin{cases} \frac{\partial \hat{c}_\xi}{\partial t} + \hat{\mathbf{v}}_\xi \cdot \hat{\nabla} \hat{c}_\xi = \hat{\nabla} \cdot (\hat{\mathbf{D}} \hat{\nabla} \hat{c}_\xi) & \hat{\mathbf{x}} \in \hat{\mathcal{B}}^\xi \\ \hat{c}_\xi = 0 & \hat{\mathbf{x}} \in \hat{\Gamma}^\xi \end{cases} \quad (6.2)$$

where  $\hat{c}_\xi(\mathbf{x})$  is particle concentration, and  $\hat{\mathbf{D}}$  the molecular diffusion coefficient. As it was done in Chapter 5, we will consider molecular diffusion to be isotropic and as such  $\hat{\mathbf{D}} = \hat{\mathcal{D}}_m \mathbf{I}$ , where  $\hat{\mathcal{D}}_m$  is the Stokes-Einstein molecular diffusion coefficient, obtained from Eq. (2.15). The boundary condition  $\hat{c}_\xi = 0$  on the solid surface  $\hat{\Gamma}^\xi$  is, as mentioned, the way to set the “perfect sink” particle deposition problem. Next, a nondimensionalization step is taken for the Stokes and continuity equations, defining the following quantities:

$$p = \frac{\hat{p} l^2}{\hat{\mu} U L}; \quad \mathbf{x} = \frac{\hat{\mathbf{x}}}{L}; \quad \mathbf{v} = \frac{\hat{\mathbf{v}}}{U},$$



where  $U$  is the system characteristic velocity (usually the superficial velocity  $U = \varepsilon v_{\xi,x}$  where  $\varepsilon$  is the porous medium porosity  $\varepsilon = |\mathcal{B}|/|Y|$ ). This results in the system

$$\begin{cases} \xi^2 \nabla^2 \mathbf{v}_\xi - \nabla p_\xi = 0 & \mathbf{x} \in \mathcal{B}^\xi \\ \nabla \cdot \mathbf{v}_\xi = 0 & \mathbf{x} \in \mathcal{B}^\xi \\ \mathbf{v}_\xi = 0 & \mathbf{x} \in \Gamma^\xi \end{cases} \quad (6.3)$$

The same operation is done for the advection-diffusion-deposition system, introducing the quantities

$$c_\xi = \frac{\hat{c}_\xi}{\bar{c}}, \quad \mathbf{D} = \frac{\hat{\mathbf{D}}}{\mathcal{D}}, \quad \hat{t}_D = \frac{L^2}{\mathcal{D}}, \quad \hat{t}_A = \frac{L}{U}, \quad t = \frac{\hat{t}}{\hat{t}_D}$$

where  $\bar{c}$  and  $\mathcal{D}$  are characteristic values for particle concentration and diffusion coefficient. Moreover, the two characteristic time-scales for advection ( $\hat{t}_A$ ) and diffusion ( $\hat{t}_D$ ) are defined as:

$$\hat{t}_A = \frac{L}{U}, \quad \hat{t}_D = \frac{L^2}{\mathcal{D}},$$

whose ratio define the Péclet number,  $Pe$ , as:

$$Pe = \frac{\hat{t}_D}{\hat{t}_A}.$$

This results in the dimensionless system

$$\begin{cases} \frac{\partial c_\xi}{\partial t} + \nabla \cdot (-\mathbf{D} \nabla c_\xi + Pe \mathbf{v}_\xi c_\xi) = 0 & \mathbf{x} \in \mathcal{B}^\xi \\ c_\xi = 0 & \mathbf{x} \in \Gamma^\xi \end{cases} \quad (6.4)$$

## 6.2 Upscaled Model

The next step is to apply the principles of the multiple-scale asymptotic expansion to the two systems (6.3) and (6.4). The procedure for the homogenization of Stokes' equation is reported in Chapter 2 (and the references mentioned therein), so it won't be reported again here: it has nevertheless to be noted that a number of results obtained in that procedure will be relevant and of use when dealing in the upscaling of the advection-diffusion equation in this chapter, and will be referenced as appropriate. As usual, the method introduces a “fast” spatial variable  $\mathbf{y}$ , to which a new time variable  $\tau_a$  is

added, defined as follows:

$$\mathbf{y} = \frac{\mathbf{x}}{\xi}, \quad \tau_a = t\text{Pe} = \frac{\hat{t}}{\hat{t}_A} \quad . \quad (6.5)$$

Then,  $c_\xi$  is represented as  $c_\xi(\mathbf{x}, t) = c(\mathbf{x}, \mathbf{y}, t, \tau_a)$ , and the latter is expanded into an asymptotic series of  $\xi$

$$c(\mathbf{x}, \mathbf{y}, t, \tau_a) = \sum_{m=0}^{\infty} \xi^m c_m(\mathbf{x}, \mathbf{y}, t, \tau_a) \quad (6.6)$$

The same expansion is also applied for the velocity vector field  $\mathbf{v}_\xi(\mathbf{x}, t)$ :

$$\mathbf{v}(\mathbf{x}, \mathbf{y}, t, \tau_a) = \sum_{m=0}^{\infty} \xi^m \mathbf{v}_m(\mathbf{x}, \mathbf{y}, t, \tau_a) \quad (6.7)$$

Replacing  $c_\xi(\mathbf{x}, t)$  with  $c(\mathbf{x}, \mathbf{y}, t, \tau_a)$  (adding the "fast" variable), leads to the following derivation rule for the spatial and temporal derivatives:

$$\nabla c_\xi = \nabla_x c + \xi^{-1} \nabla_y c, \quad (6.8)$$

$$\frac{\partial c_\xi}{\partial t} = \frac{\partial c}{\partial t} + \text{Pe} \frac{\partial c}{\partial \tau_a}. \quad (6.9)$$

We now have expressed all the coefficient functions in their form valid in the unit cell  $Y$ . Hence, for the sake of clarity and compactness, from now on (unless where needed otherwise) we will always refer to them in a shortened form: e.g.  $c_i$  instead of  $c_i(\mathbf{x}, \mathbf{y}, t, \tau_a)$ . Using (6.8) and (6.9) in (6.4) leads to:

$$\begin{cases} \frac{\partial c}{\partial t} + \text{Pe} \frac{\partial c}{\partial \tau_a} + \\ \quad + (\nabla_x + \xi^{-1} \nabla_y) \cdot (-\mathbf{D}(\nabla_x c + \xi^{-1} \nabla_y c) + \text{Pec}c) = 0 & \mathbf{y} \in \mathcal{B} \\ c = 0 & \mathbf{y} \in \Gamma \end{cases} \quad (6.10)$$

Then, using the expansions reported in Eqs. (6.6) and (6.7) (up to terms  $\mathcal{O}(\xi^2)$ ), together with setting

$$\text{Pe} = \xi^{-\alpha}, \quad (6.11)$$

the transport equation for the fluid zone  $\mathcal{B}$  reported in Eq. (6.10) becomes:

$$\begin{aligned} & \xi^0 \frac{\partial c_0}{\partial t} + \xi^1 \frac{\partial c_1}{\partial t} + \xi^2 \frac{\partial c_2}{\partial t} + \xi^{0-\alpha} \frac{\partial c_0}{\partial \tau_a} + \xi^{1-\alpha} \frac{\partial c_1}{\partial \tau_a} + \xi^{2-\alpha} \frac{\partial c_2}{\partial \tau_a} = \\ & \nabla_x \cdot \{ -\mathbf{D}[\nabla_x(\xi^0 c_0 + \xi^1 c_1 + \xi^2 c_2) + \xi^{-1} \nabla_y(\xi^0 c_0 + \xi^1 c_1 + \xi^2 c_2)] + \\ & + \xi^{-\alpha}(\xi^0 \mathbf{v}_0 + \xi^1 \mathbf{v}_1 + \xi^2 \mathbf{v}_2)(\xi^0 c_0 + \xi^1 c_1 + \xi^2 c_2) \} + \\ & + \xi^{-1} \nabla_y \cdot \{ -\mathbf{D}[\nabla_x(\xi^0 c_0 + \xi^1 c_1 + \xi^2 c_2) + \xi^{-1} \nabla_y g(\xi^0 c_0 + \xi^1 c_1 + \xi^2 c_2)] + \\ & + \xi^{-\alpha}(\xi^0 \mathbf{v}_0 + \xi^1 \mathbf{v}_1 + \xi^2 \mathbf{v}_2)(\xi^0 c_0 + \xi^1 c_1 + \xi^2 c_2) \} \end{aligned} \quad (6.12)$$

or more clearly, in order to arrange the power-like terms of  $\xi$ ,

$$\begin{aligned} & \xi^{-2} \nabla_y \cdot (-\mathbf{D} \nabla_y c_0 + \xi^{1-\alpha} \mathbf{v}_0 c_0) + \\ & \xi^{-1} \left\{ \nabla_x \cdot (-\mathbf{D} \nabla_y c_0) - \nabla_y \cdot [\mathbf{D}(\nabla_x c_0 + \nabla_y c_1)] + \right. \\ & \quad \left. + \xi^{1-\alpha} \left[ \frac{\partial c_0}{\partial \tau_a} + \nabla_x \cdot (\mathbf{v}_0 c_0) + \nabla_y \cdot (\mathbf{v}_0 c_1 + \mathbf{v}_1 c_0) \right] \right\} + \\ & + \xi^0 \left\{ \frac{\partial c_0}{\partial t} - \nabla_x \cdot [\mathbf{D}(\nabla_x c_0 + \nabla_y c_1)] - \nabla_y \cdot [\mathbf{D}(\nabla_x c_1 + \nabla_y c_2)] + \right. \\ & \quad \left. \xi^{1-\alpha} \left[ \frac{\partial c_1}{\partial \tau_a} + \nabla_x \cdot (\mathbf{v}_0 c_1 + \mathbf{v}_1 c_0) + \nabla_y \cdot (\mathbf{v}_0 c_2 + \mathbf{v}_1 c_1 + \mathbf{v}_2 c_0) \right] \right\} = \mathcal{O}(\xi) \end{aligned} \quad (6.13)$$

Similarly, the same expansion operated on the boundary condition on  $\Gamma$  of Eq. (6.10) leads to:

$$\xi^0 c_0 + \xi^1 c_1 + \xi^2 c_2 = \mathcal{O}(\xi^3) \quad \mathbf{y} \in \Gamma \quad (6.14)$$

It has to be noted that expressing the dimensionless Pe number as a function of the still dimensionless scale parameter  $\xi$  and the number  $\alpha \in \mathbb{R}$  is legitimate, and it is done for simplicity of the treatment of the Péclet number during the multiple-scale expansion procedure. Moreover, in this way a clear constraint in the homogenization of the advection-dispersion equation is identified, which is the condition that  $\alpha < 2$ , as clearly stated in [Auriault and Adler \(1995\)](#).

### Terms of order $\mathcal{O}(\xi^{-2})$

Next, we collect the leading order terms of Eqs. (6.13) and (6.14) to create a hierarchical scale of systems of equations. In the first one, terms of order

$\xi^{-2}$  and  $\xi^{-1-\alpha}$  are collected:

$$\begin{cases} (\nabla_y \cdot (-\mathbf{D}\nabla_y c_0 + \xi^{1-\alpha} \mathbf{v}_0 c_0) = 0 & \mathbf{y} \in \mathcal{B} \\ c_0 = 0 & \mathbf{y} \in \Gamma \end{cases} \quad (6.15)$$

The homogeneity of both equations in this system ensures the existence of a trivial solution, i.e.:  $c_0 = c_0(\mathbf{x})$  (and consequently  $\nabla_y c_0 = 0$ ). It has to be mentioned that the same result was obtained during the upscaling of the Stokes equation with regards to fluid pressure (Eq. (2.71)), and again this is consistent with physical intuition, as it expresses the concentration behaviour as the sum of large-(spatial)scale dynamics and fast pore-scale oscillations.

#### Terms of order $\mathcal{O}(\xi^{-1})$

Then, terms of order  $\xi^{-1}$  and  $\xi^{-\alpha}$  are collected:

$$\begin{cases} [\nabla_x \cdot (-\mathbf{D}\nabla_y c_0)] - \nabla_y \cdot [\mathbf{D}(\nabla_x c_0 + \nabla_y c_1)] + \\ \quad + \xi^{1-\alpha} \left[ \frac{\partial c_0}{\partial \tau_a} + \nabla_x (\mathbf{v}_0 c_0) + \nabla_y (\mathbf{v}_0 c_1 + \mathbf{v}_1 c_0) \right] = 0 & \mathbf{y} \in \mathcal{B} \\ c_1 = 0 & \mathbf{y} \in \Gamma \end{cases}$$

Now, we consider that, since  $\nabla_y c_0 = 0$  as obtained in the previous scale,

$$[\nabla_x \cdot (-\mathbf{D}\nabla_y c_0)] = 0. \quad (6.16)$$

Then, we integrate Eq. (6.16) over the fluid domain  $\mathcal{B}$  with respect to  $\mathbf{y}$ , resulting in:

$$\begin{aligned} \int_{\mathcal{B}} -\nabla_y \cdot [\mathbf{D}(\nabla_x c_0 + \nabla_y c_1)] d\mathbf{y} + \xi^{1-\alpha} \left( \int_{\mathcal{B}} \frac{\partial c_0}{\partial \tau_a} d\mathbf{y} + \right. \\ \left. + \int_{\mathcal{B}} \nabla_x \cdot (\mathbf{v}_0 c_0) d\mathbf{y} + \int_{\mathcal{B}} \nabla_y \cdot (\mathbf{v}_0 c_1) d\mathbf{y} + \int_{\mathcal{B}} \nabla_y \cdot (\mathbf{v}_1 c_0) d\mathbf{y} \right) = 0 \end{aligned}$$

At this point, we introduce the local volumic averages of a quantity  $\mathcal{A}(\mathbf{x})$ , as follows:

$$\langle \mathcal{A} \rangle = \frac{1}{|Y|} \int_{\mathcal{B}} \mathcal{A} dy, \quad \langle \mathcal{A} \rangle_{\mathcal{B}} = \frac{1}{|B|} \int_{\mathcal{B}} \mathcal{A} dy, \quad \langle \mathcal{A} \rangle_{\Gamma} = \frac{1}{|\Gamma|} \int_{\Gamma} \mathcal{A} dy \quad (6.17)$$

where  $\langle \mathcal{A} \rangle = \varepsilon \langle \mathcal{A} \rangle_{\mathcal{B}}$ , in order to express two of the terms in Eq. (6.17) in the

following way:

$$\int_{\mathcal{B}} \frac{\partial c_0}{\partial \tau_a} d\mathbf{y} = \frac{\partial c_0}{\partial \tau_a} \int_{\mathcal{B}} d\mathbf{y} = |\mathcal{B}| \frac{\partial c_0}{\partial \tau_a}$$

and

$$\int_{\mathcal{B}} \nabla_x \cdot (\mathbf{v}_0 c_0) d\mathbf{y} = \nabla_x c_0(\mathbf{x}) \int_{\mathcal{B}} \mathbf{v}_0 d\mathbf{y} = \nabla_x \cdot (c_0 |\mathcal{B}| \langle \mathbf{v}_0 \rangle_{\mathcal{B}})$$

Next we will use the divergence theorem and considering that thanks to the assumption about the unit cells structure made in Eq. (2.65), the boundary of the fluid domain,  $d\mathcal{B}$ , can be split in the boundary of the unit cell  $dY$  and the solid surface  $\Gamma$ :  $d\mathcal{B} = \Gamma + dY$ . This results in:

$$\int_{\mathcal{B}} \nabla_y \cdot (\mathbf{v}_0 c_1) d\mathbf{y} = \int_{\Gamma} \mathbf{n} \cdot \mathbf{v}_0 c_1 d\mathbf{y} + \int_{dY} \mathbf{n} \cdot \mathbf{v}_0 c_1 d\mathbf{y} = 0 ,$$

where the two integrals vanish due to, respectively, the no-slip condition on  $\mathbf{v}_0$  and the assumed periodicity of the coefficient functions  $\mathbf{v}_0$  and  $c_0$ . For the same reason,

$$\int_{\mathcal{B}} \nabla_y \cdot (\mathbf{v}_1 c_0) d\mathbf{y} = c_0(\mathbf{x}) \left( \int_{\Gamma} (\mathbf{n} \cdot \mathbf{v}_1) d\mathbf{y} + \int_{dY} (\mathbf{n} \cdot \mathbf{v}_1) d\mathbf{y} \right) = 0 .$$

Regarding the last term,

$$\begin{aligned} \int_{\mathcal{B}} -\nabla_y [\mathbf{D}(\nabla_x c_0 + \nabla_y c_1)] d\mathbf{y} &= - \int_{\Gamma} \mathbf{n} \cdot [\mathbf{D}(\nabla_x c_0 + \nabla_y c_1)] d\mathbf{y} - \\ &- \int_{dY} \mathbf{n} \cdot [\mathbf{D}(\nabla_x c_0 + \nabla_y c_1)] d\mathbf{y} = - \int_{\Gamma} \mathbf{n} \cdot [\mathbf{D}(\nabla_x c_0 + \nabla_y c_1)] d\mathbf{y} \end{aligned} \quad (6.18)$$

At this point it is useful to write the macroscale (in the  $\Omega$  domain) expression of the diffusive particle flux towards the grain surface  $\Gamma_{\xi}$ . With the usual assumption of Fickian transport, we can define the flux as:

$$j_{\xi} = \int_{\Gamma_{\xi}} -\mathbf{n} \cdot (\mathbf{D} \nabla c_{\xi}) d\mathbf{y} \quad (6.19)$$

and using the derivation rule in Eq. (6.8), operating the multiple-scale ex-

pansion of Eq. (6.6) and arranging the power-like terms of  $\xi$  results in:

$$\begin{aligned}
j &= \int_{\Gamma} -\mathbf{n} \cdot [\mathbf{D} \nabla_x (\xi^0 c_0 + \xi^1 c_1 + \xi^2 c_2)] d\mathbf{y} + \\
&+ \xi^{-1} \int_{\Gamma} -\mathbf{n} \cdot [\mathbf{D} \nabla_y (\xi^0 c_0 + \xi^1 c_1 + \xi^2 c_2)] d\mathbf{y} = \\
&= \xi^{-1} \int_{\Gamma} -\mathbf{n} \cdot (\mathbf{D} \nabla_y c_0) d\mathbf{y} + \\
&+ \xi^0 \int_{\Gamma} -\mathbf{n} \cdot [\mathbf{D} (\nabla_x c_0 + \nabla_y c_1)] d\mathbf{y} + \\
&+ \xi^1 \int_{\Gamma} -\mathbf{n} \cdot [\mathbf{D} (\nabla_x c_1 + \nabla_y c_2)] d\mathbf{y} + \mathcal{O}(\xi^2), \tag{6.20}
\end{aligned}$$

where the first term in  $\xi^{-1}$  vanishes due to the result from the scale of  $\xi^{-2}$ , stating that  $\nabla_y c_0 = 0$ . We can thus write the flux in a more compact way as follows:

$$\begin{aligned}
j &= \xi^0 \int_{\Gamma} -\mathbf{n} \cdot [\mathbf{D} (\nabla_x c_0 + \nabla_y c_1)] d\mathbf{y} + \xi^1 \int_{\Gamma} -\mathbf{n} \cdot [\mathbf{D} (\nabla_x c_1 + \nabla_y c_2)] d\mathbf{y} + \mathcal{O}(\xi^2) = \\
&= j_{,\varepsilon^{-1}} + j_{,\varepsilon^0}, \tag{6.21}
\end{aligned}$$

and comparing Eq. (6.18) with Eq. (6.21), the result of the  $\xi^{-1}$  term is:

$$j_{,\varepsilon^{-1}} + \xi^{1-\alpha} \left( |\mathcal{B}| \frac{\partial c_0}{\partial \tau_a} + \nabla_x (c_0 |\mathcal{B}| \langle \mathbf{v}_0 \rangle_{\mathcal{B}}) \right) = 0, \tag{6.22}$$

or

$$\xi^{1-\alpha} \frac{\partial c_0}{\partial \tau_a} = \xi^{1-\alpha} [-\nabla_x (c_0 \langle \mathbf{v}_0 \rangle_{\mathcal{B}})] - \hat{j}_{,\varepsilon^{-1}}, \tag{6.23}$$

where we defined the volumetric particle flux to the surface (from the scale  $\xi^{-1}$ ) as:

$$\hat{j}_{,\varepsilon^{-1}} = \frac{j_{,\varepsilon^{-1}}}{|\mathcal{B}|}. \tag{6.24}$$

Substituting Eq. (6.23) in the original Eq. (6.16) (before the integration step) in order to eliminate the temporal derivatives, the following is obtained:

$$\begin{aligned}
& -\nabla_y \cdot [\mathbf{D} (\nabla_x c_0 + \nabla_y c_1)] - \hat{j}_{,\varepsilon^{-1}} + \\
& + \xi^{1-\alpha} [-\nabla_x \cdot (c_0 \langle \mathbf{v}_0 \rangle_{\mathcal{B}}) + \nabla_x \cdot (\mathbf{v}_0 c_0) + \nabla_y \cdot (\mathbf{v}_0 c_1 + \mathbf{v}_1 c_0)] = 0 \tag{6.25}
\end{aligned}$$

Now, considering the  $Y$ -periodicity of  $\mathbf{v}_1$ , the no-slip condition at the scale

$\xi^1$ ,  $\nabla_y \cdot \mathbf{v}_0$  (from the continuity equation at the scale  $\xi^{-1}$ ), that  $\nabla_y \cdot \mathbf{v}_1 + \nabla_x \cdot \mathbf{v}_0 = 0$  (from the continuity equation at the scale  $\xi^0$ ), and again the result from the advection-diffusion equation at the scale  $\xi^{-2}$ , we can write some of the terms in Eq. (6.25) in the following way:

$$-\nabla_x \cdot (c_0 \langle \mathbf{v}_0 \rangle_{\mathcal{B}}) = -c_0 \nabla_x \cdot \langle \mathbf{v}_0 \rangle_{\mathcal{B}} - \langle \mathbf{v}_0 \rangle_{\mathcal{B}} \cdot \nabla_x c_0 = -\langle \mathbf{v}_0 \rangle_{\mathcal{B}} \cdot \nabla_x c_0 ,$$

$$\nabla_x \cdot (\mathbf{v}_0 c_0) = c_0 \nabla_x \cdot \mathbf{v}_0 + \mathbf{v}_0 \cdot \nabla_x c_0 ,$$

$$\begin{aligned} \nabla_y \cdot (\mathbf{v}_0 c_1 + \mathbf{v}_1 c_0) &= \mathbf{v}_0 \cdot \nabla_y c_1 + (c_1 \nabla_y \cdot \mathbf{v}_0) + \mathbf{v}_1 \cdot (\nabla_y c_0) + c_0 (\nabla_y \cdot \mathbf{v}_1) = \\ &= \mathbf{v}_0 \cdot (\nabla_y c_1) + c_0 (\nabla_y \cdot \mathbf{v}_1) , \end{aligned}$$

which, substituted in Eq. (6.25) and coupled with the “perfect-sink” boundary condition for the scale  $\xi^1$ , result in the system

$$\begin{cases} -\hat{j}_{,\varepsilon^{-1}} - \nabla_y \cdot [\mathbf{D}(\nabla_x c_0 + \nabla_y c_1)] + \\ \quad + \xi^{1-\alpha} [(\mathbf{v}_0 - \langle \mathbf{v}_0 \rangle_{\mathcal{B}}) \cdot \nabla_x c_0 + \mathbf{v}_0 \cdot \nabla_y c_1] = 0 & \mathbf{y} \in \mathcal{B} \\ c_1 = 0 & \mathbf{y} \in \Gamma \end{cases} \quad (6.26)$$

Then, in order to obtain a suitable cell problem, we look for a solution in the form of Eq. (2.52), such as

$$c_1(\mathbf{x}, \mathbf{y}, t, \tau_a) = \chi(\mathbf{y}) \cdot \nabla_x c_0(\mathbf{x}, t, \tau_a) + \bar{c}_1(\mathbf{x}, t, \tau_a) \quad (6.27)$$

leading to:

$$\nabla_y c_1 = \nabla_x c_0 \cdot \nabla_y \chi , \quad (6.28)$$

Substitution in Eq. (6.26) leads to:

$$\begin{cases} -\hat{j}_{,\varepsilon^{-1}} + \nabla_x c_0 \cdot [-(\nabla_y \mathbf{D}) \cdot (\nabla_y \chi + \mathbf{I}) + \xi^{1-\alpha} \mathbf{v}_0 \nabla_y \chi] = \\ \quad = \xi^{1-\alpha} [(\langle \mathbf{v}_0 \rangle_{\mathcal{B}} - \mathbf{v}_0) \cdot \nabla_x c_0] & \mathbf{y} \in \mathcal{B} \\ \chi(\mathbf{y}) \cdot \nabla_x c_0 + \bar{c}_1 = 0 & \mathbf{y} \in \Gamma \end{cases} \quad (6.29)$$

This boundary value problem has a clear coupling between the pore-scale and the macroscopic scale, as the solution  $\chi(\mathbf{y})$  still has a dependency on the macroscopic particle concentration  $c_0(\mathbf{x})$ . This inconsistency is solved

by eliminating the dependence of  $\chi(\mathbf{y})$  on  $\nabla_x c_0$  by defining  $\chi(\mathbf{y})$  to be the  $Y$ -periodic solution of the cell problem:

$$\begin{cases} -\nabla_y \mathbf{D}(\nabla_y \chi + \mathbf{I}) + \boxed{\frac{1}{|\mathcal{B}|} \int_{\Gamma} \mathbf{n} \cdot \mathbf{D}(\nabla_y \chi + \mathbf{I}) d\Gamma} + \\ \quad + \xi \text{Pe} \mathbf{v}_0 \nabla_y \chi = \xi \text{Pe} (\langle \mathbf{v}_0 \rangle_{\mathcal{B}} - \mathbf{v}_0) & \mathbf{y} \in \mathcal{B} \\ \chi(\mathbf{y}) = 0 & \mathbf{y} \in \Gamma \end{cases} \quad (6.30)$$

where the highlighted part is the partial volumetric surface particle flux  $\hat{j}_{,\varepsilon^{-1}}$ :

$$\hat{j}_{,\varepsilon^{-1}} = \frac{1}{|\mathcal{B}|} \int_{\Gamma} \mathbf{n} \cdot \mathbf{D}(\nabla_y \chi + \mathbf{I}) d\Gamma \quad (6.31)$$

No additional constraints to upscaling arise, apart from the already mentioned  $\alpha > 2$  to guarantee homogenizability and  $\xi \ll \frac{l}{L}$  to ensure scale separation. Thus, we can get to a form of the macroscale effective transport equation by moving up one step in the hierarchy of scales, to scale  $\xi^0$ .

### Terms of order $\mathcal{O}(\xi^0)$

The terms of order  $\xi^0$  and  $\xi^{1-\alpha}$  in Eq. (6.13) are collected:

$$\begin{cases} \frac{\partial c_0}{\partial t} - \nabla_x \cdot [\mathbf{D}(\nabla_x c_0 + \nabla_y c_1)] - \nabla_y \cdot [\mathbf{D}(\nabla_x c_1 + \nabla_y c_2)] + \\ \quad \xi^{1-\alpha} \left[ \frac{\partial c_1}{\partial \tau_a} + \nabla_x \cdot (\mathbf{v}_0 c_1 + \mathbf{v}_1 c_0) + \nabla_y \cdot (\mathbf{v}_0 c_2 + \mathbf{v}_1 c_1 + \mathbf{v}_2 c_0) \right] = 0 & \mathbf{y} \in \mathcal{B} \\ c_2 = 0 & \mathbf{y} \in \Gamma \end{cases} \quad (6.32)$$

Again, we integrate Eq. (6.32) over  $\mathcal{B}$  with respect to  $\mathbf{y}$  resulting in, term by term:

$$\int_{\mathcal{B}} \frac{\partial c_0}{\partial t} dy = |\mathcal{B}| \frac{\partial \langle c_0 \rangle_{\mathcal{B}}}{\partial t} ;$$

then, using Eq. (6.27),

$$\begin{aligned} -\nabla_x \cdot [\mathbf{D}(\nabla_x c_0 + \nabla_y c_1)] &= -\nabla_x \cdot [\mathbf{D}(\nabla_x c_0 + \nabla_y \chi \cdot \nabla_x c_0)] \\ &= -\nabla_x [\cdot \mathbf{D} \nabla_x c_0 (\nabla_y \chi + \mathbf{I})] \end{aligned}$$



which, integrated over  $\mathcal{B}$ , reads:

$$\begin{aligned} \int_{\mathcal{B}} -\nabla_x \cdot \mathbf{D} \nabla_x c_0 (\nabla_y \chi + \mathbf{I}) dy &= -\nabla_x \cdot \nabla_x c_0 |\mathcal{B}| \langle \mathbf{D} \cdot (\nabla_y \chi + \mathbf{I}) \rangle_{\mathcal{B}} = \\ &= -\nabla_x \cdot \mathbf{D}^{**} \nabla_x c_0 |Y| \end{aligned}$$

where  $\mathbf{D}^{**} = \langle \mathbf{D} \cdot (\nabla_y \chi + \mathbf{I}) \rangle$ . Then,

$$\int_{\mathcal{B}} \frac{\partial c_1}{\partial \tau_a} dy = |\mathcal{B}| \frac{\partial \langle c_1 \rangle_{\mathcal{B}}}{\partial \tau_a}$$

and

$$\int_{\mathcal{B}} \nabla_x \cdot (\mathbf{v}_0 c_1 + \mathbf{v}_1 c_0) dy = |\mathcal{B}| \nabla_x \cdot (\langle c_1 \mathbf{v}_0 \rangle_{\mathcal{B}} + c_0 \langle \mathbf{v}_1 \rangle_{\mathcal{B}}) .$$

and

$$\begin{aligned} \int_{\mathcal{B}} \nabla_y \cdot (\mathbf{v}_0 c_2 + \mathbf{v}_1 c_1 + \mathbf{v}_2 c_0) dy &= \\ \int_{\mathcal{B}} \nabla_y \cdot (\mathbf{v}_0 c_2) dy + \int_{\mathcal{B}} \nabla_y \cdot (\mathbf{v}_1 c_1) dy + \int_{\mathcal{B}} \nabla_y \cdot (\mathbf{v}_2 c_0) dy &= 0. \end{aligned}$$

It can be immediately proven that this integral vanishes, using the divergence theorem as done earlier and considering the no-slip conditions for  $\mathbf{v}_0, \mathbf{v}_1$  and  $\mathbf{v}_2$  coming from the different expanded scales of the boundary condition on  $\Gamma$  of Eq. (2.70), and the periodicity on the boundary  $dY$  of coefficient functions  $\mathbf{v}_1, \mathbf{v}_2, c_1$  and  $c_2$ . Finally, the last term

$$\int_{\mathcal{B}} (\nabla_y \cdot \mathbf{D} (\nabla_x c_1 + \nabla_y c_2)) dy$$

can be treated much in the same way as Eq. (6.18) and, comparing it to Eqs. (6.20), (6.21), we have:

$$\int_{\mathcal{B}} (\nabla_y \cdot \mathbf{D} (\nabla_x c_1 + \nabla_y c_2)) dy = - \int_{\Gamma} \mathbf{n} \cdot \mathbf{D} (\nabla_x c_1 + \nabla_y c_2) dy = j_{,\varepsilon^0}$$

Hence, the result of the  $\xi^0$  term is:

$$\begin{aligned} &|\mathcal{B}| \frac{\partial \langle c_0 \rangle_{\mathcal{B}}}{\partial t} - \nabla_x \cdot \mathbf{D}^{**} \nabla_x c_0 |Y| + j_{,\varepsilon^0} \\ &+ \xi^{1-\alpha} \left( |\mathcal{B}| \frac{\partial \langle c_1 \rangle_{\mathcal{B}}}{\partial \tau_a} + |\mathcal{B}| \nabla_x \cdot (\langle c_1 \mathbf{v}_0 \rangle_{\mathcal{B}} + c_0 \langle \mathbf{v}_1 \rangle_{\mathcal{B}}) \right) = 0 . \end{aligned}$$

Then, with

$$\hat{j}_{,\varepsilon^0} = \frac{\dot{j}_{,\varepsilon^0}}{|\mathcal{B}|} \quad (6.33)$$

and rearranging the terms by powers of  $\xi$  and dividing by volume  $\mathcal{B}$ , we have:

$$\frac{\partial \langle c_0 \rangle_{\mathcal{B}}}{\partial t} - \nabla_x \cdot (\varepsilon^{-1} \mathbf{D}^{**} \cdot (\nabla_x c_0)) + \hat{j}_{,\varepsilon^0} + \xi^{1-\alpha} \left( \frac{\partial \langle c_1 \rangle_{\mathcal{B}}}{\partial \tau_a} + \nabla_x (\langle c_1 \mathbf{v}_0 \rangle_{\mathcal{B}} + c_0 \langle \mathbf{v}_1 \rangle_{\mathcal{B}}) \right) = 0 \quad (6.34)$$

Since  $\mathbf{v}_0 = -\mathbf{k}(\mathbf{y}) \nabla_x p_0$ , where  $\mathbf{k}(\mathbf{y}) = \frac{w_j(\mathbf{y})}{\mu}$  as expressed in Eq. (2.76),

$$\begin{aligned} \langle c_1 \mathbf{v}_0 \rangle_{\mathcal{B}} &= \langle (\chi(\mathbf{y}) \cdot \nabla_x c_0 + \bar{c}_1) \mathbf{v}_0 \rangle_{\mathcal{B}} = \langle (\chi(\mathbf{y}) \cdot \nabla_x c_0) \mathbf{v}_0 + \bar{c}_1 \mathbf{v}_0 \rangle_{\mathcal{B}} = \\ &= \langle \chi(\mathbf{y}) \cdot \mathbf{k}(\mathbf{y}) \rangle_{\mathcal{B}} \cdot (\nabla_x p_0 \otimes \nabla_x c_0) + \bar{c}_1 \langle \mathbf{v}_0 \rangle_{\mathcal{B}}. \end{aligned}$$

Since  $\langle \mathcal{A} \rangle_{\mathcal{B}} = \langle \mathcal{A} \rangle |Y| / |\mathcal{B}|$ , and defining a new effective dispersion coefficient  $\mathbf{D}^* = \mathbf{D}^{**} + \xi \text{Pe} \langle \chi \mathbf{k} \rangle \nabla_x p_0$ , we obtain

$$\frac{\partial \langle c_0 \rangle_{\mathcal{B}}}{\partial t} + \xi^{1-\alpha} \frac{\partial \langle c_1 \rangle_{\mathcal{B}}}{\partial \tau_a} = \nabla_x \cdot (\varepsilon^{-1} \mathbf{D}^* \cdot \nabla_x c_0) - \varepsilon^{-1} \xi^{1-\alpha} \nabla_x (c_0 \langle \mathbf{v}_1 \rangle + \bar{c}_1 \langle \mathbf{v}_0 \rangle) - \hat{j}_{,\varepsilon^0} \quad (6.35)$$

Now, using:

$$\frac{\partial \langle c_{\xi} \rangle_{\mathcal{B}}}{\partial t} = \frac{\partial \langle c \rangle_{\mathcal{B}}}{\partial t} + \text{Pe} \frac{\partial \langle c \rangle_{\mathcal{B}}}{\partial \tau_a}$$

and

$$\langle c \rangle_{\mathcal{B}} = \langle c_0 \rangle_{\mathcal{B}} + \xi \langle c_1 \rangle_{\mathcal{B}} + \mathcal{O}(\xi^2)$$

leads to:

$$\frac{\partial \langle c \rangle_{\mathcal{B}}}{\partial t} = \frac{\partial \langle c_0 \rangle_{\mathcal{B}}}{\partial t} + \xi \frac{\partial \langle c_1 \rangle_{\mathcal{B}}}{\partial t} + \xi^{-\alpha} \left( \frac{\partial \langle c_0 \rangle_{\mathcal{B}}}{\partial \tau_a} + \xi \frac{\partial \langle c_1 \rangle_{\mathcal{B}}}{\partial \tau_a} \right),$$

and multiplying by  $\xi$ , to:

$$\xi \frac{\partial \langle c \rangle_{\mathcal{B}}}{\partial t} = \xi^{1-\alpha} \frac{\partial \langle c_0 \rangle_{\mathcal{B}}}{\partial \tau_a} + \xi \left( \frac{\partial \langle c_0 \rangle_{\mathcal{B}}}{\partial t} + \xi^{1-\alpha} \frac{\partial \langle c_1 \rangle_{\mathcal{B}}}{\partial \tau_a} \right) + \mathcal{O}(\xi^2) \quad (6.36)$$

Now, multiplying Eq. (6.35) by  $\xi$ , and adding the results to Eq. (6.22), and using the result from Eq. (6.36), the following expression is obtained:

$$\begin{aligned} \xi \frac{\partial \langle c_0 \rangle_{\mathcal{B}}}{\partial t} + \xi \xi^{1-\alpha} \frac{\partial \langle c_1 \rangle_{\mathcal{B}}}{\partial \tau_a} + \xi^{1-\alpha} \frac{\partial c_0}{\partial \tau_a} = \\ \xi \nabla_x (\varepsilon^{-1} \mathbf{D}^* \cdot \nabla_x c_0) - \varepsilon^{-1} \xi \xi^{1-\alpha} \nabla_x (c_0 \langle \mathbf{v}_1 \rangle + \\ + \bar{c}_1 \langle \mathbf{v}_0 \rangle) + \xi^{1-\alpha} (-\nabla_x c_0 \langle \mathbf{v}_0 \rangle_{\mathcal{B}} - \hat{j}_{,\varepsilon^{-1}} - \xi \hat{j}_{,\varepsilon^0}) \end{aligned} \quad (6.37)$$

We can immediately compare the left hand side of this last equation with Eq. (6.36), and since  $c_0 = \langle c_0 \rangle_{\mathcal{B}}$  (due to  $\nabla_y c_0 = 0$ ),

$$\begin{aligned} \xi \frac{\partial \langle c \rangle_{\mathcal{B}}}{\partial t} = \xi \nabla_x (\varepsilon^{-1} \mathbf{D}^* \cdot \nabla_x \langle c_0 \rangle_{\mathcal{B}}) - \varepsilon^{-1} \xi^{1-\alpha} \nabla_x \cdot (\langle c_0 \rangle_{\mathcal{B}} \langle \mathbf{v}_0 \rangle_{\mathcal{B}} + \xi c_0 \langle \mathbf{v}_1 \rangle + \xi \bar{c}_1 \langle \mathbf{v}_0 \rangle) \\ - (\hat{j}_{,\varepsilon^{-1}} + \xi \hat{j}_{,\varepsilon^0}). \end{aligned} \quad (6.38)$$

Now, it is self evident that

$$\langle c_0 \rangle_{\mathcal{B}} \langle \mathbf{v}_0 \rangle_{\mathcal{B}} = \langle c_0 \rangle_{\mathcal{B}} \langle \mathbf{v}_0 \rangle$$

which, via the usual expansion of both functions, becomes:

$$\langle c \rangle_{\mathcal{B}} \langle \mathbf{v} \rangle = \langle c_0 \rangle_{\mathcal{B}} \langle \mathbf{v}_0 \rangle + \xi \langle c_0 \rangle_{\mathcal{B}} \langle \mathbf{v}_1 \rangle + \xi \langle c_1 \rangle_{\mathcal{B}} \langle \mathbf{v}_0 \rangle + \mathcal{O}(\xi^2)$$

We can now expand  $\langle c \rangle_{\mathcal{B}}$  in this way:

$$\xi \langle c \rangle_{\mathcal{B}} = \xi \langle c_0 \rangle_{\mathcal{B}} + \mathcal{O}(\xi^2),$$

and thus can express the diffusive term in Eq. (6.38) in terms of  $\langle c \rangle_{\mathcal{B}}$  which, (after dividing by  $\xi$  and multiplying by  $\varepsilon$ ), becomes:

$$\varepsilon \frac{\partial \langle c \rangle_{\mathcal{B}}}{\partial t} = \nabla_x \cdot (\mathbf{D}^* \cdot \nabla_x \langle c \rangle_{\mathcal{B}}) - \text{Pe} \nabla_x \cdot (\langle c \rangle_{\mathcal{B}} \langle \mathbf{v} \rangle) - \tilde{j} \cdot \frac{1}{\xi} \quad (6.39)$$

where  $\tilde{j} = \varepsilon \hat{j} = \varepsilon (\hat{j}_{,\varepsilon^{-1}} + \xi \hat{j}_{,\varepsilon^0})$ . This is the final form of the upscaled equation, approximated up to the order  $\xi^2$ . Unfortunately, this expression does not constitute a proper macroscale expression for advective-diffusive-reactive transport, as the term  $\tilde{j}$  still shows a dependence on the coefficient functions  $c_0$ ,  $c_1$  and  $c_2$ , which themselves are defined in terms of both the slow and the fast variables  $\mathbf{x}$  and  $\mathbf{y}$ , whereas a proper macroscale formulation has to ignore the features and oscillatory behaviour at the pore-scale and as such, show no dependence on  $\mathbf{y}$ .

### 6.3 Conclusions

In this final chapter we changed the perspective with which we approached the issue of obtaining an appropriate predictive model for the particle deposition problem. In the previous part of this thesis we analyzed fluid flow and particle transport at the microscopic level by means of accurate numerical simulations, at certain operating conditions and in different porous media with specific features, and subsequently using the information gained at the microscale to build predictive models employable at the macroscopic scale. In this chapter instead, the method of asymptotic homogenization via multiple-scale expansion was employed, in order to obtain a upscaled formulation within a purely theoretical framework. First of all, we made the assumption that the fluid flow follows Stokes' equation of motion: this is legitimate for a very wide range of practical cases, such as flow in aquifers. This was done in order to build our analysis upon a well-known and established result of homogenization theory, providing for a robust procedure for the upscaling of Stokes' equation, and an example of the framework in which the following steps were taken. Next, the pore-scale formulation of the advection-diffusion reaction was given, with the particle deposition problem expressed (as explained in Chapter (5) in the form of a Dirichlet boundary condition of particle concentration equal to zero at the border of the grains. Then, in the hierarchy of problems coming from the asymptotic expansion, a cell problem was identified, the solution of which would provide for the determination of the effective particle transport coefficients in the upscaled transport equation, obtained in the last step of the procedure. This work was then successful, inasmuch it was possible to obtain a final formulation of the particle advection-diffusion-reaction where a source term (not present in the original, pore-scale, formulation) appears, which refers to the macroscale removal of particles in the porous medium due to deposition phenomena. Nevertheless, in the current form of this equation the macroscale source term still shows a dependence on the microscale coefficient functions describing the behaviour of particle concentration at the pore-scale, and is thus not readily employable. More work is thus needed to obtain an appropriate formulation of this term, in a way that ignores the details of the microscopic structure and only depends on the length scales of the full system. Finally, when this last step will have been solved, the framework has already been developed in order to solve the proposed cell problem with microscale methods (e.g.: CFD) and obtain the upscaled transport coefficients, thus connecting the methodology employed in the remainder of this thesis with a rigorous and robust method of transport equations upscaling.

## Chapter 7

# Conclusions

In this dissertation, the investigation of particle and scalar transport and reaction, or deposition, in porous media is discussed. The approach chosen in this work has been to explore the nature of fluid flow and particle transport and deposition performing detailed computational fluid dynamics (CFD) simulations of these phenomena, by using accurate reproductions of the microscopic structure of the packings considered. In addition to CFD simulations, also the methodology to obtain the geometric models was fully “artificial”, that is, the structure of the porous media investigated was algorithmically reconstructed with rigid-body simulations reproducing the actual process of the packing formation. Moreover, we placed great emphasis on the use of free and open-source codes and software in this work, in order to maximize the reproducibility of the results and the easiness of furthering the development of the techniques proposed herein.

Chapter 2 gives a theoretical background on the nature of studying porous media and specifically on the issue of their inherent multiscale nature. The equations for fluid flow, scalar and particle transport in saturated media are stated, along with their corresponding classic upscaled form. Then, the problem of particle surface deposition is introduced, along with a description of current state of the research. The equivalence of the investigation of this problem and that of surface reactions involving scalars is also mentioned. The limitations coming from the statement of this problem in the form of simplified geometrical models are made clear, manifesting the need for detailed pore-scale simulations.

Thus, in Chapter 3 the first results coming from pore-scale simulations of single phase flow and scalar transport are shown. Only one porous medium model was considered, but wide ranges of Reynolds and Péclet numbers have been investigated, including non-linear regimes. In this initial approach to

detailed microscale simulations, great care was given in the pre-processing phase and mesh construction process, in order to ensure the highest possible accuracy with respect to numerical and computational issues, often encountered when solving the Navier-Stokes and the advection-diffusion equation with the finite-volume method. In order to ascertain the applicability of this methodology, all the basic features of the resulting geometric structure and fluid flow and scalar transport are analysed. Permeability, mean tortuosity, and mean shear rate have been calculated explicitly from the flow field results, while the dispersivity has been estimated both with the method of moments and using the least-square formulation of the inverse problem. The results demonstrate the validity of the method, predicting the linear and non-linear regimes of Darcy's law with well-defined permeability and tortuosity constants in the first regime, and three different regimes for hydrodynamic dispersion at increasing Péclet numbers: one dominated by the molecular dispersion, then a region where the mechanical and molecular dispersion are of the same order of magnitude, and finally a region where the inertial effects dominate. This correlation for the hydrodynamic dispersion in terms of Péclet number is verified for the porous medium under study with the proposed simulation and upscaling tools. The asymptotic dispersion regime is quickly reached and dispersion is well approximated by the Fickian hypothesis, even if the fluid velocity distributions are not Gaussian. In this chapter, the viability of artificially constructed porous media in CFD simulations has been proved, but the rigid-body simulation method was employed for just one geometric model.

The capabilities of this technique were explored in much greater detail in Chapter 4, where a variety of realistic systems describing a wide variety of catalytic bed packings characterized by different size distributions and catalyst shape were investigated. Catalytic particles in the shape of spheres, cylinders and trilobes were considered. The software **Blender** was used which, integrated with the Bullet Physics Library, provided for the rigid body simulation code with which to obtain the geometric models. This work showed how the main advantage of this approach (versus other alternatives) stands in the possibility of simulating packings constituted by particles with complex shapes (e.g. non-convex objects such as trilobes). First, the geometrical features of the artificial packings were compared to corresponding experimental data, and this demonstrated that the generated packings realistically describe the behaviour of catalytic fixed bed reactors, for instance with respect to the resulting bulk porosity. Interesting results are also obtained regarding the influence of the grains polydispersity on the resulting packing bulk porosity, where while for spherical and cylindrical particles the

expected inversely proportional relationship is found, this is not true in the case of trilobes. Finally, when working with spherical particles and cylindrical beads, the well known radial porosity profiles are obtained, with an accuracy superior to other similar tools. Having positively validated this methodology with regards to geometrical features of the packings, pressure drop simulations were carried out. These also showed very good agreement with the predictions of the Ergun law, both in the case of spherical and cylindrical catalyst shape, but also in the case of polydisperse trilobes very good results are obtained, especially considering that these complex non-convex objects are very difficult to treat. The results obtained in this Chapter show that this approach can be used to more deeply study the effect that the shape, size and length distribution of catalyst particles have on fluid flow in fixed bed reactors, and improve existing models for pressure drop predictions.

Chapter 5 comprises the last part of this thesis dealing with microscale CFD simulations. There, the study is extended to consider particle deposition, or equivalently scalar surface reaction. As mentioned earlier, the issue of the currently used models for treating particle deposition is their reliance on simplified descriptions for the porous medium, which cannot accurately describe the real pore structure, with clear effects on the predictive capabilities for this models. Thus for validation purposes, we firstly considered one single spherical collector, with Brownian motion as the dominant mechanism for deposition. In this case the original correlation proposed by Levich was obtained, thus proving the consistency of the methodology adopted with the underlying theory. Then, we took steps of increasing complexity of the porous medium model investigated. When considering complex porous media constituted by a random arrangement of different circular collectors a power-law dependency analogous to the Levich one (albeit, with different coefficients), is found. In this case porosity and effective grain size were capable of fully characterizing the observed behaviour. Then, packings constituted by irregularly shaped collectors are considered. In this case, a similar dependency was again observed although porosity and effective grain size seem not to be capable alone to fully characterize the porous medium. This deviation arising in the case of realistic geometries would seem to indicate that another parameter should be included in the laws predicting Brownian particle deposition, and is a clear indication of the failure of simple classic particle deposition models in the treatment of packings of realistic collectors. This issue also arises in the case of particle interception, where the results of the microscale simulations clearly manifest a dependency of the deposition efficiency on the Reynolds number, which the classic models do

not consider.

Chapter 6 closes this dissertation with a more theoretical approach to the problem of obtaining an appropriate upscaled form of the equations governing scalar and particle transport at the pore-scale, where the method of asymptotic homogenization via multiple-scale expansion was employed. Given the usual pore-scale formulation of the advection-diffusion reaction, we introduced the scalar/particle deposition problem, as in the preceding Chapter, with a boundary condition of particle concentration equal to zero at the walls of the solid grains. Using this procedure, it was possible to formally separate the scales of this problem in two distinct scales. First, a microscale cell problem was identified, then the final upscaled form of the original pore-scale problem is obtained, whose effective transport coefficients are the result of the solution of the cell problem. The final result proposed in this Chapter is a formulation of the particle advection-diffusion-reaction where the particle removal is not expressed as a boundary condition on the grains walls anymore (as the geometric structure details are lost in the macroscale equation), but as a source term depending on particle concentration. Further work is still needed on the formulation of this source term, as it was not yet possible to express it only as a function of macroscopic quantities, but still shows a dependence on the pore-scale coefficient functions, making it unsuitable for the use in a fully macroscale transport equation. Finally, it has to be noted that this homogenization method, obtaining an upscaled equation whose effective coefficients are obtained from the solution of an identified cell problem, pairs very well with the methodology and techniques presented in the rest of this thesis, where efficient and reliable methods for the solution of microscale scalar and particle transport and deposition problems are shown.

Concluding, this work proves the success and viability of a fully in-silico open-source approach for the investigation of multi-phase packed systems via rigid-body simulations and computational fluid dynamics.



# Bibliography

- Adamczyk, Z., Dabros, T., Czarnecki, J., Ven, T.V.D., 1983. Particle transfer to solid surfaces. *Advances in Colloid and Interface Science* 19, 183 – 252.
- Adler, R.J., Taylor, J.E., 2007. *Random fields and geometry*. Springer-Verlag, Chichester, GBR.
- Allaire, G., 1989. Homogenization of the stokes flow in a connected porous medium. *Asymptotic Analysis* 2, 203–222.
- Aris, R., 1956. On the dispersion of a solute in a fluid flowing through a tube. *Proceedings of the Royal Society of London. Series A. Mathematical and Physical Sciences* 235, 67–77.
- Asano, K., 2006. *Mass Transfer: From Fundamentals to Modern Industrial Applications*. Wiley-VCH Verlag GmbH & Co. KGaA, Weinheim, DEU.
- Augier, F., Idoux, F., Delenne, J., 2010a. Numerical simulations of transfer and transport properties inside packed beds of spherical particles. *Chemical Engineering Science* 65, 1055 – 1064.
- Augier, F., Koudil, A., Royon-Lebeaud, A., Muszynski, L., Yanouri, Q., 2010b. Numerical approach to predict wetting and catalyst efficiencies inside trickle bed reactors. *Chemical Engineering Science* 65, 255 – 260.
- Auriault, J., 1991. Heterogeneous medium. is an equivalent macroscopic description possible? *International Journal of Engineering Science* 29, 785 – 795.
- Auriault, J.L., Adler, P., 1995. Taylor dispersion in porous media: analysis by multiple scale expansions. *Advances in Water Resources* 18, 217–226.
- Battiato, I., Tartakovsky, D., 2011. Applicability regimes for macroscopic models of reactive transport in porous media. *Journal of contaminant hydrology* 120, 18–26.

- Battiato, I., Tartakovsky, D.M., Tartakovsky, A.M., Scheibe, T., 2009. On breakdown of macroscopic models of mixing-controlled heterogeneous reactions in porous media. *Advances in water resources* 32, 1664–1673.
- Bear, J., 1988. *Dynamics of fluids in porous media*. Dover, New York, USA.
- Bear, J., Bachmat, Y., 1967. Generalized theory on hydrodynamic dispersion in porous media. *Int. Union Geod. Geophys. Publ.* 72.
- Bensoussan, A., Papanicolau, G., Lions, J.L., 1980. *Asymptotic analysis for periodic structures*. North-Holland, Amsterdam, NLD.
- Bird, R., Stewart, W., Lightfoot, E., 1960. *Transport Phenomena*. Wiley, New York, USA.
- Blöcher, G., Zimmermann, G., 2008. Settle3d: a numerical generator for artificial porous media. *Computers & Geosciences* 34, 1827–1842.
- Blunt, M.J., Bijeljic, B., Dong, H., Gharbi, O., Iglauer, S., Mostaghimi, P., Paluszny, A., Pentland, C., 2013. Pore-scale imaging and modelling. *Advances in Water Resources* 51, 197–216.
- Boccardo, G., Del Plato, L., Marchisio, D., Augier, F., Haroun, Y., Ferre, D., Icardi, M., 2014a. Pore-scale simulation of fluid flow in packed-bed reactors via rigid-body simulations and cfd, in: 10th International Conference on CFD in Oil&Gas, Metallurgical and Process Industries, SINTEF, June 17-19 2014, Trondheim, NOR.
- Boccardo, G., Marchisio, D., Sethi, R., 2014b. Microscale simulation of particle deposition in porous media. *Journal of Colloid and Interface Science* 417, 227–237.
- Boyer, C., Volpi, C., Ferschneider, G., 2007. Hydrodynamics of trickle bed reactors at high pressure: Two-phase flow model for pressure drop and liquid holdup, formulation and experimental validation. *Chemical Engineering Science* 62, 7026 – 7032.
- Brenner, H., 1961. The slow motion of a sphere through a viscous fluid towards a plane surface. *Chemical Engineering Science* 16, 242 – 251.
- Cignoni, P., Callieri, M., Corsini, M., Dellepiane, M., Ganovelli, F., Ranzuglia, G., 2008. Meshlab: an open-source mesh processing tool, in: Eurographics Italian Chapter Conference, The Eurographics Association, July 2-4 2008, Salerno, ITA. pp. 129–136.

- Cioranescu, D., Donato, P., 2000. Introduction to homogenization. Oxford University Press, Oxford, GBR.
- Clennell, M.B., 1997. Tortuosity: a guide through the maze. Geological Society, London, Special Publications 122, 299–344.
- Coumans, E., 2006. Bullet physics library. Source: [bulletphysics.org](http://bulletphysics.org). Last retrieved on 10/03/2014 .
- Cushing, R.S., Lawler, D.F., 1998. Depth filtration: fundamental investigation through three-dimensional trajectory analysis. Environmental Science & Technology 32, 3793–3801.
- Cushman, J.H., Bennethum, L.S., Hu, B.X., 2002. A primer on upscaling tools for porous media. Advances in Water Resources 25, 1043–1067.
- Darcy, H., 1856. Les fontaines publiques de la ville de Dijon. Dalmont, Paris.
- Di Molfetta, A., Sethi, R., 2012. Ingegneria degli acquiferi. Springer-Verlag, Milan, ITA.
- Duda, A., Koza, Z., Matyka, M., 2011. Hydraulic tortuosity in arbitrary porous media flow. Physical Review E 84, 036319.
- Dudgeon, C., 1966. An experimental study of the flow of water through coarse granular media. La Houille Blanche 7 , 785–801.
- Einstein, A., 1905. Über die von der molekularkinetischen Theorie der Wärme geforderte Bewegung von in ruhenden Flüssigkeiten suspendierten Teilchen. Annalen der Physik 322, 549–560.
- Elimelech, M., 1991. Kinetics of capture of colloidal particles in packed beds under attractive double layer interactions. Journal of Colloid and Interface Science 146, 337–352.
- Elimelech, M., 1994. Particle deposition on ideal collectors from dilute flowing suspensions: Mathematical formulation, numerical solution, and simulations. Separations Technology 4, 186 – 212.
- Elimelech, M., Gregory, J., Jia, X., Williams, R.A., 1995. Particle Deposition and Aggregation. Butterworth-Heinemann, Woburn, MA, USA.
- Feder, J., 1980. Random sequential adsorption. Journal of Theoretical Biology 87, 237–254.

- Forchheimer, P., 1901. Wasserbewegung durch boden. Zeitschrift Verein Deutscher Ingenieure 45, 1782–1788.
- Giese, M., Rottschfer, K., Vortmeyer, D., 1998. Measured and modeled superficial flow profiles in packed beds with liquid flow. AIChE Journal 44, 484–490.
- Goren, S.L., O’Neill, M.E., 1971. On the hydrodynamic resistance to a particle of a dilute suspension when in the neighbourhood of a large obstacle. Chemical Engineering Science 26, 325 – 338.
- Happel, J., 1958. Viscous flow in multiparticle systems: Slow motion of fluids relative to beds of spherical particles. AIChE Journal 4, 197–201.
- Hassanizadeh, S.M., Gray, W., 1987. High velocity flow in porous media. Transport in Porous Media 2, 521–531.
- Hill, R., Koch, D., 2002. The transition from steady to weakly turbulent flow in a close-packed ordered array of spheres. Journal of Fluid Mechanics 465, 59–97.
- Hill, R., Koch, D., Ladd, A., 2001a. The first effects of fluid inertia on flows in ordered and random arrays of spheres. Journal of Fluid Mechanics 448, 213–241.
- Hill, R., Koch, D., Ladd, A., 2001b. Moderate-reynolds-number flows in ordered and random arrays of spheres. Journal of Fluid Mechanics 448, 243–278.
- Hornung, U., 1997. Homogenization and porous media. Springer-Verlag, New York, USA.
- Icardi, M., Boccardo, G., Marchisio, D.L., Tosco, T., Sethi, R., 2014. Pore-scale simulation of fluid flow and solute dispersion in three-dimensional porous media. Phys. Rev. E 90, 013032.
- Johnson, W.P., Li, X., Yal, G., 2007. Colloid retention in porous media: mechanistic confirmation of wedging and retention in zones of flow stagnation. Environmental Science & Technology 41, 1279–1287.
- Keller, A.A., Auset, M., 2007. A review of visualization techniques of biocolloid transport processes at the pore scale under saturated and unsaturated conditions. Advances in Water Resources 30, 1392 – 1407.

- Konstandopoulos, A., Kostoglou, M., Skaperdas, E., Papaioannou, E., Dimitrios, Z., Eudoxia, K., 2000. Fundamental studies of diesel particulate filters: Transient loading, regeneration and aging. SAE Technical Paper 2000-01-1016 .
- Koponen, A., Kataja, M., Timonen, J., 1996. Tortuous flow in porous media. *Physical Review E* 54, 406.
- Koutsourelakis, P.S., Deodatis, G., 2005. Simulation of binary random fields with applications to two-phase random media. *Journal of Engineering Mechanics* 131, 397–412.
- Kuwabara, S., 1959. The forces experienced by randomly distributed parallel circular cylinders or spheres in a viscous flow at small reynolds numbers. *Journal of the Physical Society of Japan* 14, 527–532.
- Levich, V.G., 1962. *Physicochemical Hydrodynamics*. Prentice-Hall, Englewood Cliffs, NJ, USA.
- Logan, B., Jewett, D., Arnold, R., Bouwer, E., O'Melia, C., 1995. Clarification of clean-bed filtration models. *Journal of Environmental Engineering* 121, 869–873.
- Long, W., Hilpert, M., 2009. A correlation for the collector efficiency of brownian particles in clean-bed filtration in sphere packings by a lattice-boltzmann method. *Environmental Science and Technology* 43, 4419–4424.
- Long, W., Huang, H., Serlemitsos, J., Liu, E., Reed, A.H., Hilpert, M., 2010. Pore-scale study of the collector efficiency of nanoparticles in packings of nonspherical collectors. *Colloids and Surfaces A: Physicochemical and Engineering Aspects* 358, 163 – 171.
- Lorensen, W.E., Cline, H.E., 1987. Marching cubes: A high resolution 3d surface construction algorithm, in: *ACM Siggraph Computer Graphics*, ACM. pp. 163–169.
- Ma, H., Hradisky, M., Johnson, W.P., 2013. Extending applicability of correlation equations to predict colloidal retention in porous media at low fluid velocity. *Environmental Science and Technology* 47, 2272–2278.
- Ma, H., Johnson, W.P., 2010. Colloid retention in porous media of various porosities: Predictions by the hemispheres-in-cell model. *Langmuir* 26, 1680–1687.

- Ma, H., Pedel, J., Fife, P., Johnson, W.P., 2010. Hemispheres-in-cell geometry to predict colloid deposition in porous media. *Environmental Science & Technology* 44, 4383–4383.
- van Milligen, B.P., Bons, P.D., 2012. Analytical model for tracer dispersion in porous media. *Physical Review E* 85, 011306.
- Nelson, K.E., Ginn, T.R., 2005. Colloid filtration theory and the happel sphere-in-cell model revisited with direct numerical simulation of colloids. *Langmuir* 21, 2173–2184.
- OpenCFD, 2013. The Open Source CFD Toolbox, User Guide. OpenCFD (ESI). Source: [www.openfoam.org](http://www.openfoam.org). Last retrieved: 31/09/2014.
- Øren, P.E., Bakke, S., 2002. Process based reconstruction of sandstones and prediction of transport properties. *Transport in Porous Media* 46, 311–343.
- Palencia, E.S., 1980. Non-homogeneous media and vibration theory. Springer-Verlag, Berlin, DEU.
- Pazmino, E., H., M., Johnson, W., 2011. Applicability of colloid filtration theory in size-distributed, reduced porosity, granular media in the absence of energy barriers. *Environmental Science and Technology* 45, 10401–10407.
- Pfeffer, R., 1964. Heat and mass transport in multiparticle systems. *Industrial & Engineering Chemistry Fundamentals* 3, 380–383.
- Pilotti, M., 1998. Generation of realistic porous media by grains sedimentation. *Transport in Porous Media* 33, 257–278.
- Prieve, D.C., Ruckenstein, E., 1974. Effect of london forces upon the rate of deposition of brownian particles. *AIChE Journal* 20, 1178–1187.
- Rajagopalan, R., Tien, C., 1976. Trajectory analysis of deep-bed filtration with the sphere-in-cell porous media model. *AIChE Journal* 22, 523–533.
- Sahimi, M., 1995. Effect of long-range correlations on transport phenomena in disordered media. *AIChE Journal* 41, 229–240.
- Sahimi, M., 2012. Flow and Transport in Porous Media and fractured rock. Wiley, Weinheim, DEU.

- Schneebeli, G., 1955. Expériences sur la limite de validité de la loi de darcy et l'apparition de la turbulence dans un écoulement de filtration. *La Houille Blanche*, 141–149.
- Sethi, R., 2011. A dual-well step drawdown method for the estimation of linear and non-linear flow parameters and wellbore skin factor in confined aquifer systems. *Journal of Hydrology* 400, 187 – 194.
- Spielman, L.A., Fitzpatrick, J.A., 1973. Theory for particle collection under london and gravity forces. *Journal of Colloid and Interface Science* 42, 607 – 623.
- Tartar, L., 1980. Incompressible fluid flow in a porous medium-convergence of the homogenization process. Appendix of [16]. T. Muthukumar Department of Mathematics, Indian Institute of Science, Bangalore-560012, India E-mail address: tmk@math.iisc.ernet.in .
- Tosco, T., Marchisio, D., Lince, F., Sethi, R., 2013. Extension of the darcy-forchheimer law for shear-thinning fluids and validation via pore-scale flow simulations. *Transport in Porous Media* 96, 1–20.
- Tufenkji, N., Elimelech, M., 2004. Correlation equation for predicting single-collector efficiency in physicochemical filtration in saturated porous media. *Environmental Science & Technology* 38, 529–536.
- Van Gumster, J., 2009. *Blender For Dummies*. Wiley, Hoboken, NJ, USA.
- Whitaker, S., 1999. *The method of volume averaging*. Kluwer, Dordrecht, NLD.
- Yao, K.M., 1968. Influence of suspended particle size on the transport aspect of water filtration. Ph.D. thesis. University of North Carolina, Chapel Hill, NC, USA.
- Yao, K.M., Habibian, M.T., O'Melia, C.R., 1971. Water and waste water filtration. concepts and applications. *Environmental Science & Technology* 5, 1105–1112.
- Yeong, C., Torquato, S., 1998. Reconstructing random media. *Physical Review E* 57, 495–507.
- Zhikov, V., Kozlov, S., Olejnik, O., 1994. Homogenization of differential operators and integral functionals. Transl. from the Russian by G. A. Yosifian. Springer-Verlag, Berlin, DEU.

- Zou, R., 1995. The packing of spheres in a cylindrical container: the thickness effect. *Chemical Engineering Science* 50, 1504–1507.